# Supplementary Information

# Accurate stacking engineering of MOF nanosheets as membranes for precise H$_2$ sieving

Wufeng Wu[1#], Xitai Cai[1#], Xianfeng Yang[2], Yanying Wei[1✉], Li Ding[3], Libo Li[1✉], Haihui Wang[3✉]

[1]School of Chemistry and Chemical Engineering, Guangdong Provincial Key Lab of Green Chemical Product Technology, State Key Laboratory of Pulp and Paper Engineering, South China University of Technology, Guangzhou 510640, China

[2]Analytical and Testing Centre, South China University of Technology, Guangzhou 510640, China

[3]Beijing Key Laboratory for Membrane Materials and Engineering, Department of Chemical Engineering, Tsinghua University, Beijing 100084, China

[#]These authors contributed equally: Wufeng Wu, Xitai Cai

[✉]e-mail address: ceyywei@scut.edu.cn; celbli@scut.edu.cn; cehhwang@tsinghua.edu.cn

**This PDF file includes:**

Supplementary Methods

Supplementary Figures 1 to 32

Supplementary Tables 1 to 11

Supplementary References

## Supplementary Methods

**Materials.** All used chemical regents without further purification were received from the commercial suppliers. Copper(II) nitrate hydrate ($Cu(NO_3)_2 \cdot 3H_2O$, 99.99%) was obtained from Aladdin. 2,5-dihydroxyterephthalic acid (BDC-$(OH)_2$, 98%), 2,5-dibromoterephthalic acid (BDC-$(Br)_2$, 98%), nitroterephthalic acid (BDC-$NO_2$, 98%), acetonitrile (99.5%) and dichloromethane ($CH_2Cl_2$, 99.5%) were obtained from Macklin. N,N-dimethylformamide (DMF, 99%) was obtained from RichJoint Chemical Reagents Co., China. α-Alumina (α-$Al_2O_3$) support was obtained from Foshan Yirun fine ceramic new material Co., China.

**Theoretical calculation**. The density functional theory (DFT) method as implemented with Vienna Ab initio Simulation Package (VASP 6.1.0)[1,2] was used to perform the structural optimization and calculate the formation energy. We adopted Perdew-Burke-Ernzerhof (PBE) exchange-correlation functional[3] including DFT-D3 dispersion correction with Becke-Johnson (BJ) damping scheme[4], an approach that is widely used in DFT calculations[5-9] and high-throughput screenings[10,11] of various MOFs for its reliability and accuracy. The plane-wave basis set with an energy cut-off of 1000 eV and Gaussian smearing with a smearing width of 0.05 eV were utilized for the calculation. The Brillouin zone was sampled with the Monkhorst-Pack scheme. To be specific, a 3×2×5 k-point mesh and a 2×2×3 k-point mesh were used for bulk phase and nanosheet calculation, respectively. The energy convergence criterion for the self-consistent field (SCF) approach was $10^{-5}$ eV. Both atomic positions and lattice parameters were fully optimized with the conjugate gradient algorithm until the atomic forces were less than 0.05 eV/Å. The optimized bulk phase structures and the crystal data are shown in Supplementary Fig. 1 and Supplementary Table 1, respectively.

To explore the stacking stability of CuBDC-X nanosheets, where X represented -$(OH)_2$, -$(Br)_2$, -$NH_2$, -$NO_2$, -OH and -Br, the formation energy as a function of stacking modes were evaluated by the climbing-image nudged elastic band (CI-NEB) method[12]. As shown in Fig. 1a, we considered a pathway in which the bilayer CuBDC-X nanosheet slid from AA-stacked to AB-stacked mode and 4 images along the sliding pathway were employed. The force convergence criterion for the CI-NEB calculation was 0.05 eV/Å. The formation energy ($E_{form}$) was calculated as:

$$E_{form} = E_{\text{bilayer}} - 2E_{\text{monolayer}} \qquad (1)$$

where $E_{\text{bilayer}}$ and $E_{\text{monolayer}}$ represented the potential energy of the stacked CuBDC-X nanosheet and the monolayer CuBDC-X, respectively. The calculated $E_{form}$ was illustrated in Fig. 1c and Supplementary Figs. 2-6. The crystal data for the optimized geometries were listed in Supplementary Tables 2-7. Furthermore, the Widom test particle insertion method[13] and Monte Carlo (MC) simulations as implemented with RASPA2[14] software package were performed to calculate the isosteric heat of adsorption ($Q_{st}$) at infinite dilution and 2D density distributions for gases within the stacked CuBDC-X nanosheets, respectively. The Lennard-Jones (LJ) interactions were truncated at 14.0 Å with analytical tail corrections to estimate interactions beyond the cutoff distance. The electrostatic interactions were treated using the Ewald summation method[15]. The stacked CuBDC-X nanosheets were described by the UFF4MOF force field[16,17], corresponding partial charges of framework atoms were calculated using the DDEC6 approach[18]. Gas molecules of $CO_2$, $N_2$ and $CH_4$ were described by the TraPPE force field[19], while the $H_2$ gas molecule was described using the force field developed by Snurr and coworkers[20]. The adsorption amount of gas molecules at 1 bar and 298.15 K was calculated by Grand canonical MC simulations consisting of 200,000 cycles, with the first 100,000 cycles for equilibrium and subsequent 100,000 cycles for ensemble averages. After that, canonical MC simulations were conducted to obtain 2D density distributions over 100,000 Monte Carlo cycles, as shown in Supplementary Fig. 27. The heat

of adsorption at infinite dilution was shown in Fig. 4c and Supplementary Fig. 25 .

To obtain the dipole moment of linkers, the structural optimization of linker molecules was firstly performed with Gaussian16[6] at the B3LYP/6-311+G(d) level of theory. The dipole moment of linkers was then calculated with Multiwfn program[21].

Various distance/size data are given in detail, including the side-chain size of linker, aperture of monolayer MOF nanosheet, stacking aperture ($\varphi_{stack}$) and interlayer distance ($d$-spacing) of neighboring MOF nanosheets. As shown in Fig. 2, the side-chain size in linker is measured by calculating the distance from the carbon atom attached to a group on the linker to the furthest atom of the group (considering the van der Waals radii of the atoms involved). The aperture of a monolayer MOF nanosheet is defined as the in-plane pore size of the monolayer nanosheet. The $\varphi_{stack}$ represents the aperture of neighboring MOF nanosheets stacked at the lowest formation energy. The $\varphi_{stack}$ and the monolayer aperture were calculated using the Zeo++ software[22]. The $d$-spacing value, which represents the interlayer distance of neighboring nanosheets, is determined by measuring the vertical distance between the centers of mass of the two layers.

**Calculation of Miller indices**. Detailed calculations for $hkl$ are given as follows[23]:

A lattice point in the reciprocal lattice $\mathbf{g}_{hkl}$ can be described as:

$$\mathbf{g}_{hkl} = h\mathbf{a}^* + k\mathbf{b}^* + l\mathbf{c}^* \tag{2}$$

where $hkl$ are called Miller indices. Each reciprocal lattice point $hkl$ (reflection or diffraction spot) represents a set of parallel planes (called Bragg planes) in real space. The orientation of the planes is determined by the Miller indices $hkl$, perpendicular to the reciprocal lattice vector $\mathbf{g}_{hkl}$. These planes cut the unit-cell axes an integer number of times per unit cell. Each Miller index tells us how many times a given set of planes cut a unit-cell axis. Each set of planes has its specific index.
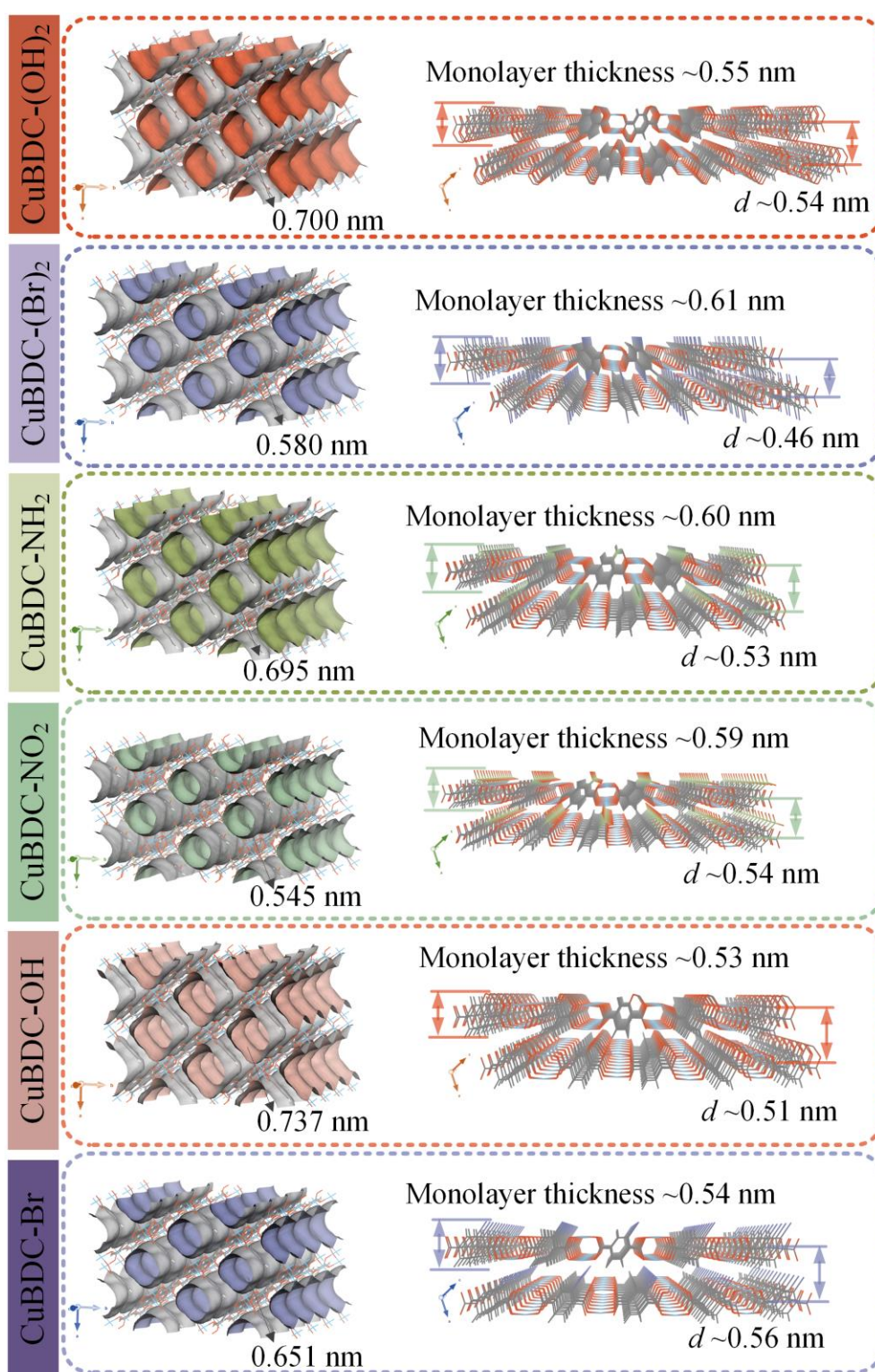
The interplanar distance $d_{hkl}$, is inversely proportional to the length of the reciprocal lattice vector $\mathbf{g}_{hkl}$

$$d_{hkl} = {1}/{|\mathbf{g}_{hkl}|} \tag{3}$$

Where

$$\mathbf{g}_{hkl}^2 = \frac{1}{d_{hkl}^2} = h^2\mathbf{a}^{*2} + k^2\mathbf{b}^{*2} + l^2\mathbf{c}^{*2} + 2kl\mathbf{b}^*\mathbf{c}^*cos\alpha^* +$$

$$2hl\mathbf{a}^*\mathbf{c}^*cos\beta^* + 2hk\mathbf{a}^*\mathbf{b}^*cos\gamma^* \tag{4}$$
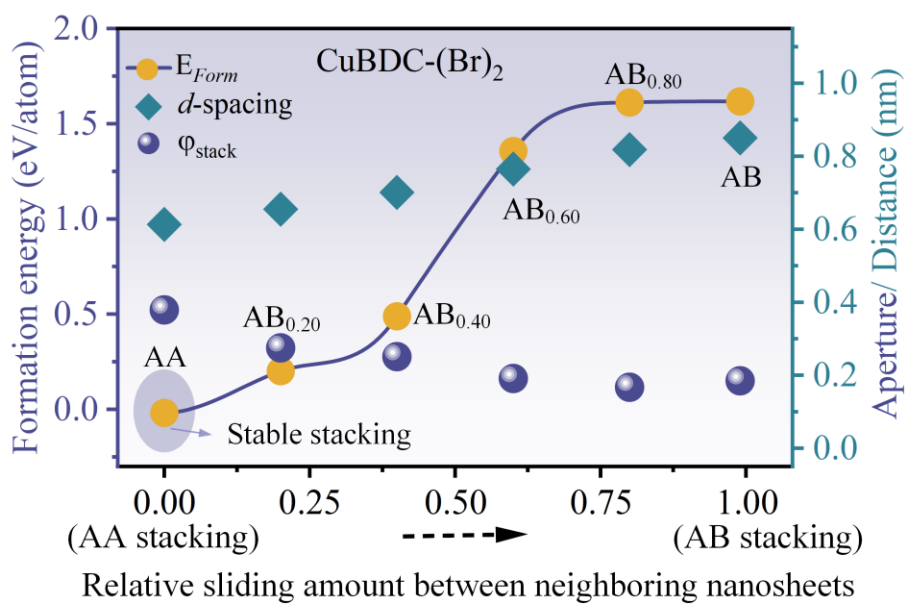
# Supplementary Figures



**Supplementary Fig. 1. Crystalline structures of bulk MOFs.** The crystalline structures of bulk CuBDC-(OH)$_2$, CuBDC-(Br)$_2$, CuBDC-NH$_2$, CuBDC-NO$_2$, CuBDC-OH and CuBDC-Br optimized by DFT viewed along different directions, showing theoretical monolayer thickness, $d$-spacing ($d$) and monolayer nanosheet aperture. C, O, Cu, N, Br and H atoms are colored in gray, red, blue, green, purple and gray, respectively.
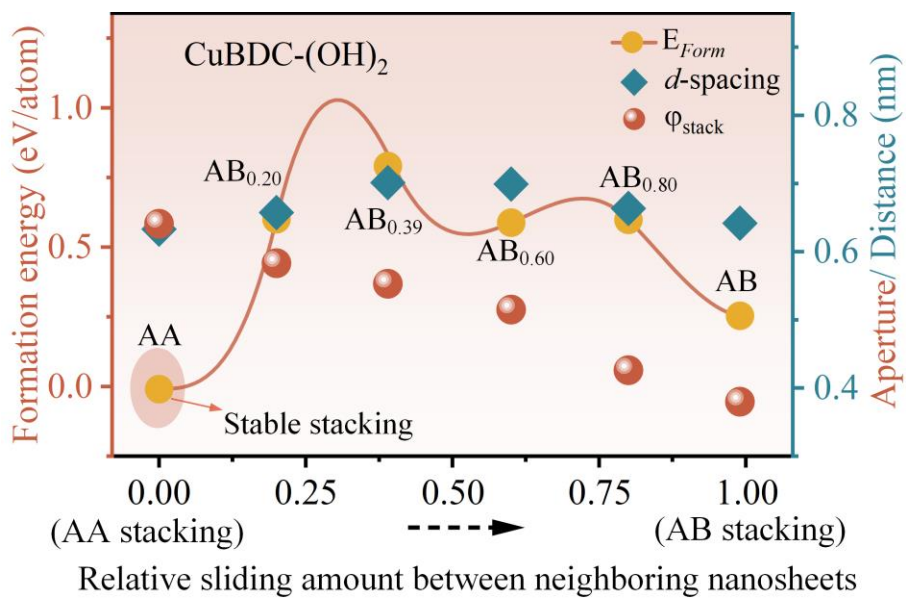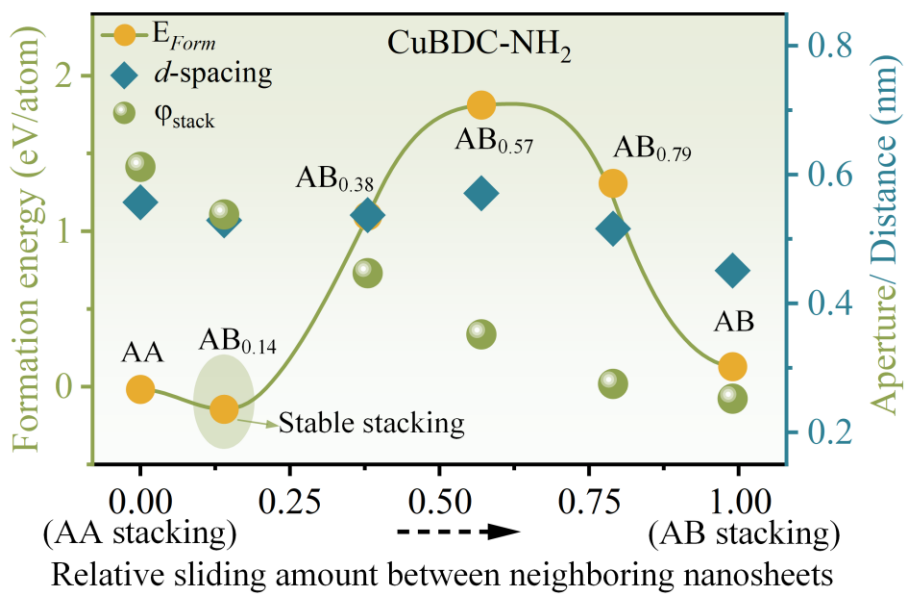
**Supplementary Fig. 2. Sliding path of neighboring stacked CuBDC-(OH)$_2$ nanosheets.** Different stacking modes of CuBDC-(OH)$_2$ nanosheets, corresponding to different formation energy (E$_{form}$), $d$-spacing and effective stacking aperture ($\varphi_{stack}$).

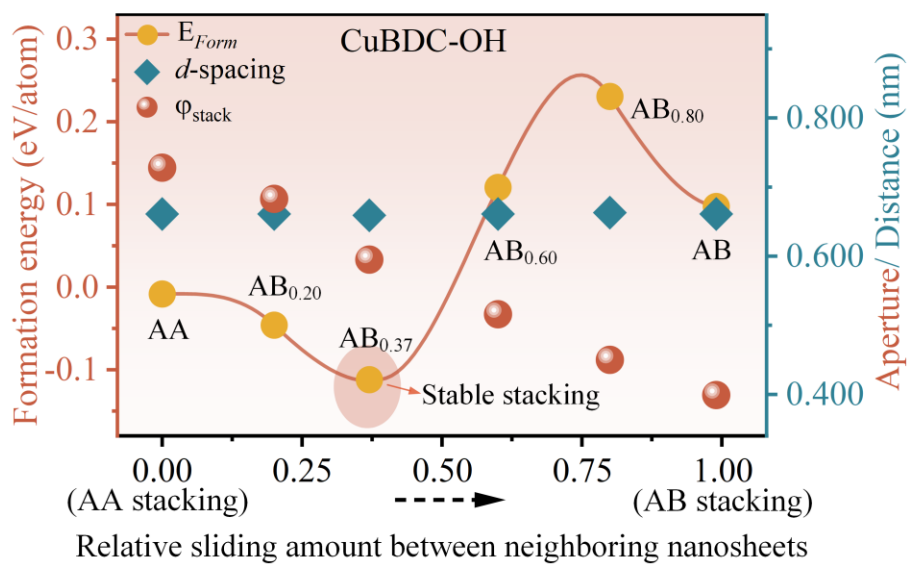**Supplementary Fig. 3. Sliding path of neighboring stacked CuBDC-(Br)₂ nanosheets.** Different stacking modes of CuBDC-(Br)₂ nanosheets, corresponding to different formation energy (E$_{form}$), $d$-spacing and effective stacking aperture ($\varphi_{stack}$).
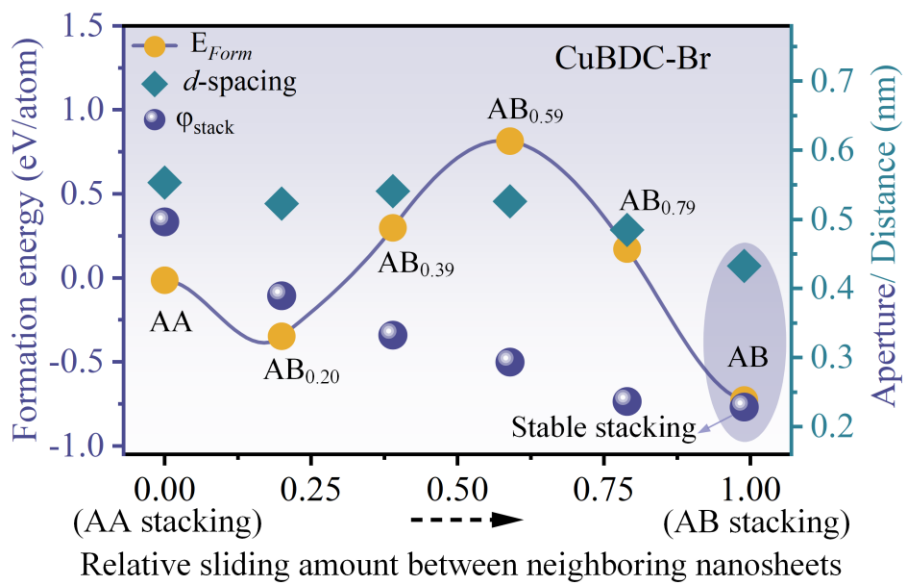
**Supplementary Fig. 4. Sliding path of neighboring stacked CuBDC-NH₂ nanosheets.** Different stacking modes of CuBDC-NH₂ nanosheets, corresponding to different formation energy ($E_{form}$), $d$-spacing and effective stacking aperture ($\varphi_{stack}$).

**Supplementary Fig. 5. Sliding path of neighboring stacked CuBDC-OH nanosheets.** Different stacking modes of CuBDC-OH nanosheets, corresponding to different formation energy ($E_{form}$), $d$-spacing and effective stacking aperture ($\varphi_{stack}$).

**Supplementary Fig. 6. Sliding path of neighboring stacked CuBDC-Br nanosheets.**
Different stacking modes of CuBDC-Br nanosheets, corresponding to different formation energy ($E_{form}$), $d$-spacing and effective stacking aperture ($\varphi_{stack}$).
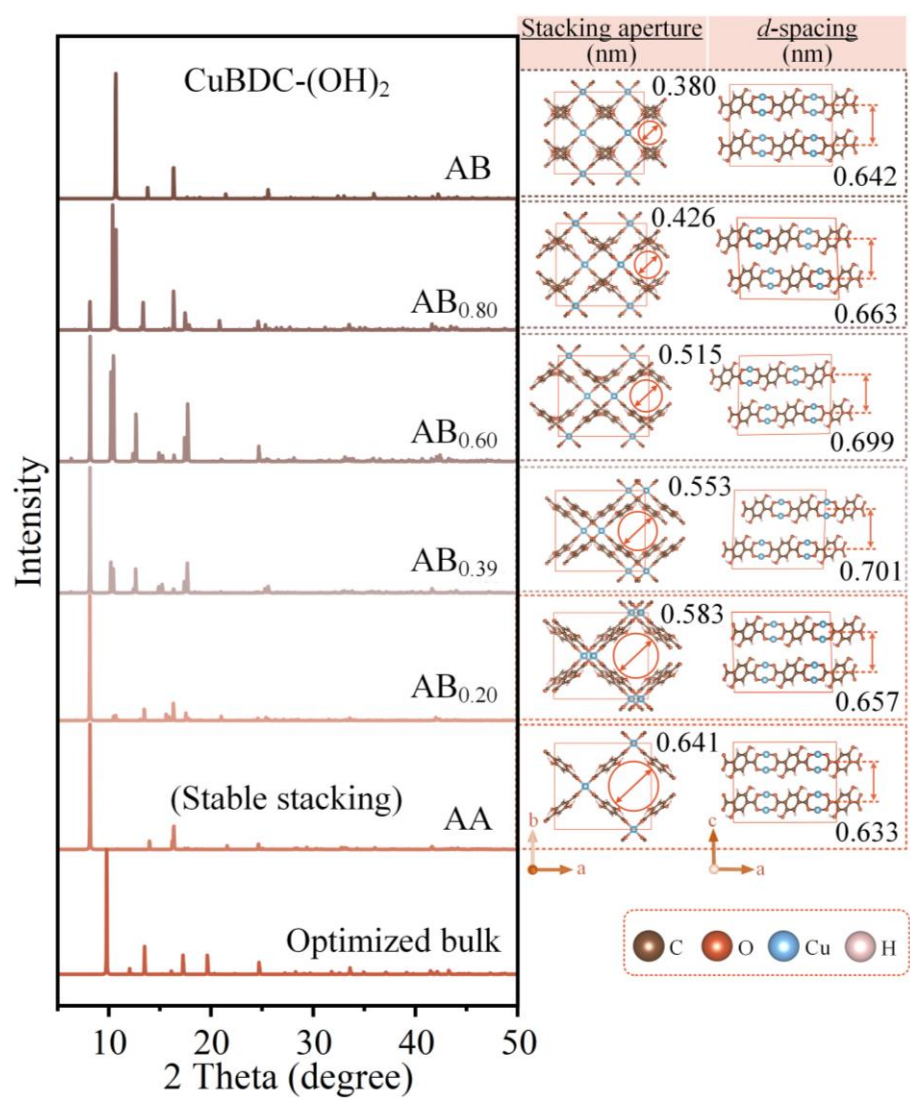
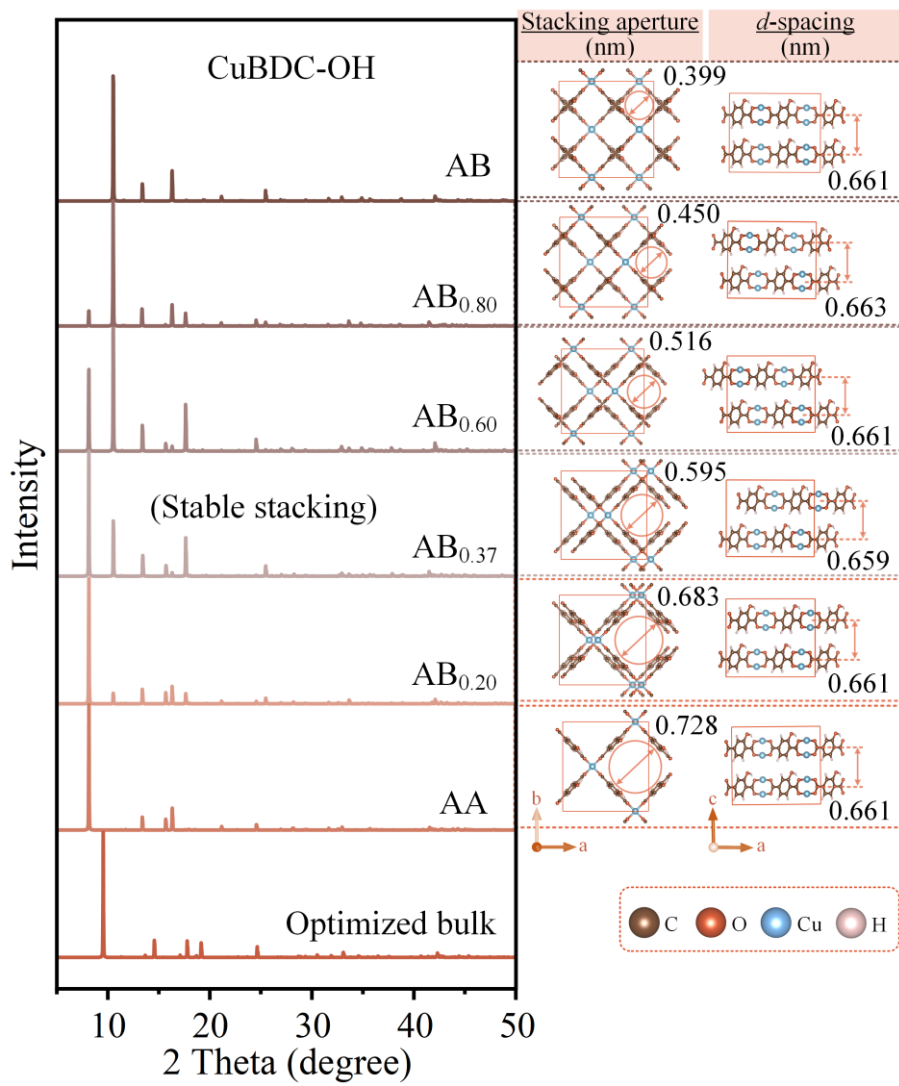**Supplementary Fig. 7.** Simulated XRD patterns and stacking structures along various projections of the CuBDC-(OH)$_2$ nanosheets with different stacking modes, and corresponding stacking aperture with various *d*-spacing.
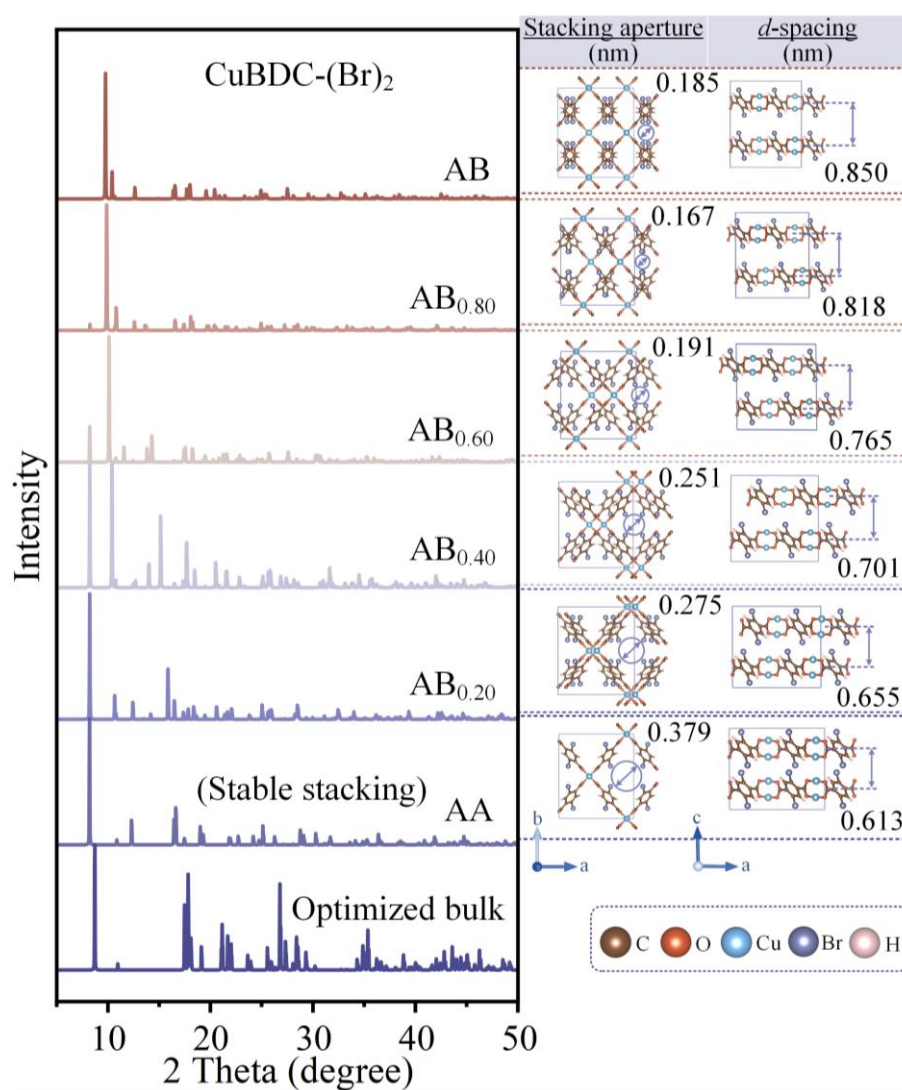
**Supplementary Fig. 8.** Simulated XRD patterns and stacking structures along various projections of the CuBDC-(Br)$_2$ nanosheets with different stacking modes, and corresponding stacking aperture with various *d*-spacing.
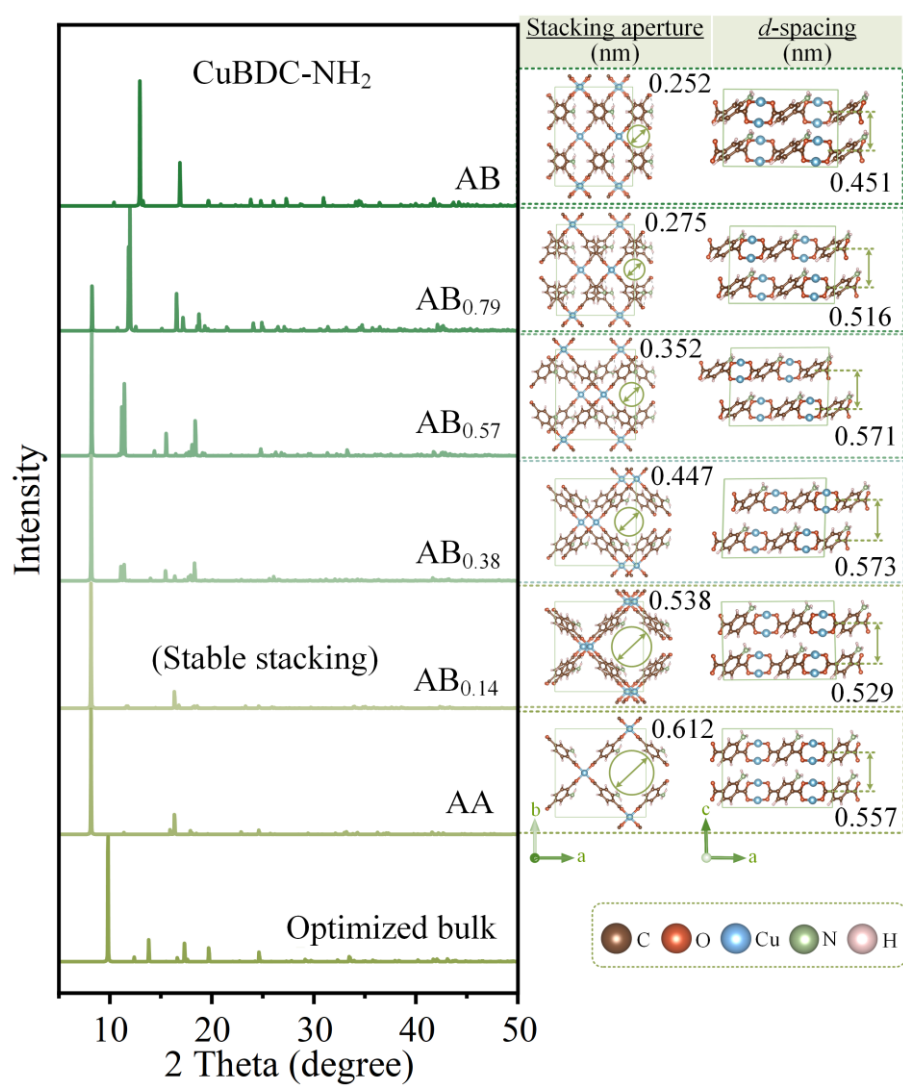
**Supplementary Fig. 9.** Simulated XRD patterns and stacking structures along various projections of the CuBDC-NH$_2$ nanosheets with different stacking modes, and corresponding stacking aperture with various $d$-spacing.

**Supplementary Fig. 10.** Simulated XRD patterns and stacking structures along various projections of the CuBDC-OH nanosheets with different stacking modes, and corresponding stacking aperture with various *d*-spacing.
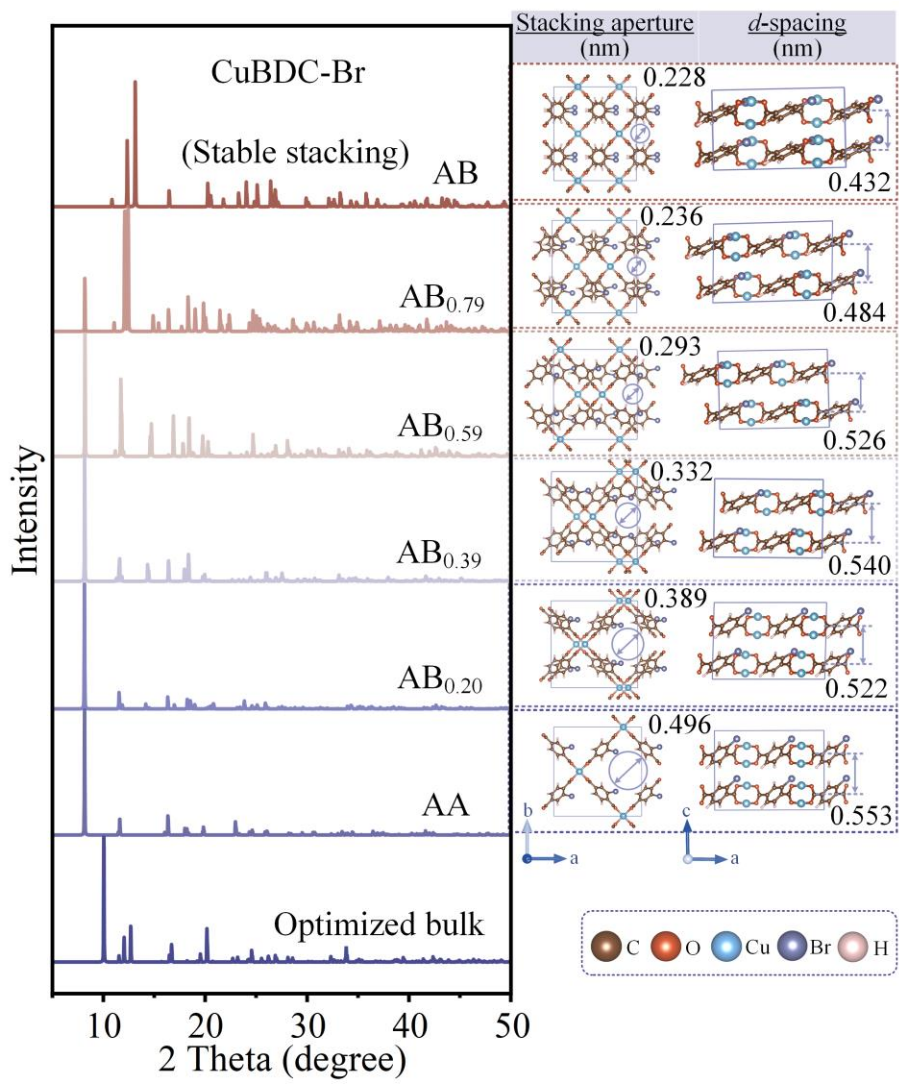
**Supplementary Fig. 11.** Simulated XRD patterns and stacking structures along various projections of the CuBDC-Br nanosheets with different stacking modes, and corresponding stacking aperture with various *d*-spacing.
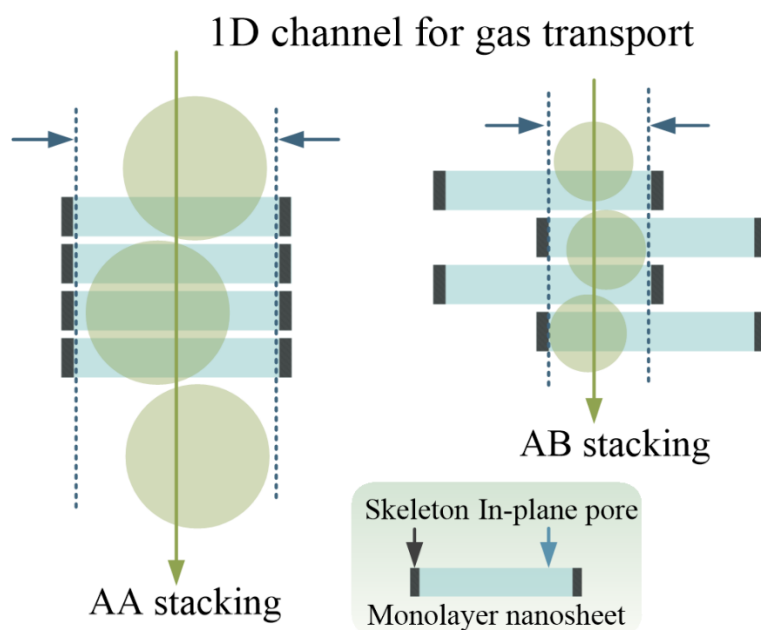
**Supplementary Fig. 12. Scheme of gas transport through AA and AB stacked MOF nanosheets.** Considering the narrow free spacing (< 0.2 nm) between neighboring MOF nanosheets where gas molecules are not allowed to pass, gas molecules can only transport through the one-dimensional (1D) vertical channels constructed by in-plane pores of stacked MOF nanosheets in the membrane. For AA stacking, the neighboring nanosheets are highly overlapped, allowing gas molecules to pass through relatively larger 1D channels. The AB stacking structure with the maximum staggered degree between neighboring nanosheets results in the formation of relatively smaller gas transport channels.
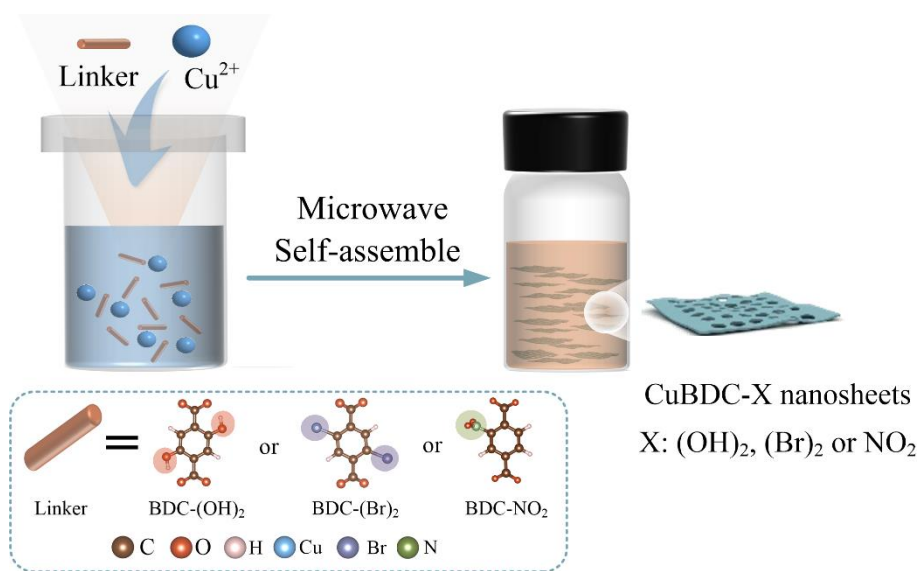
**Supplementary Fig. 13.** Schematic of microwave synthesis of CuBDC-$(OH)_2$, CuBDC-$(Br)_2$ and CuBDC-$NO_2$ nanosheets.
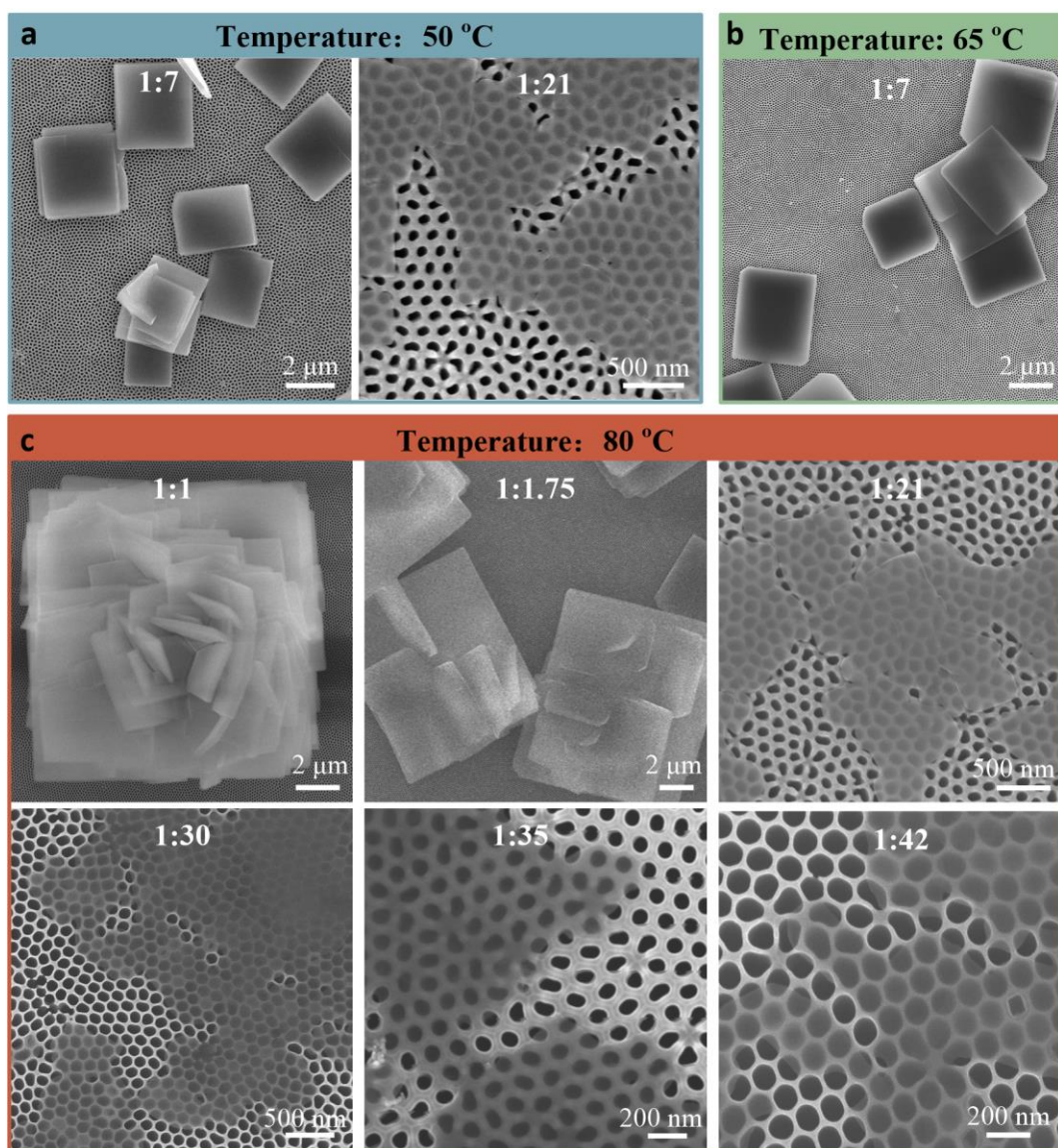
**Supplementary Fig. 14.** The SEM images of the CuBDC-(Br)$_2$ nanosheets prepared under different reaction conditions. Values of Cu/linker ratio and reaction temperature are given, with all reactions carried out for 30 min.
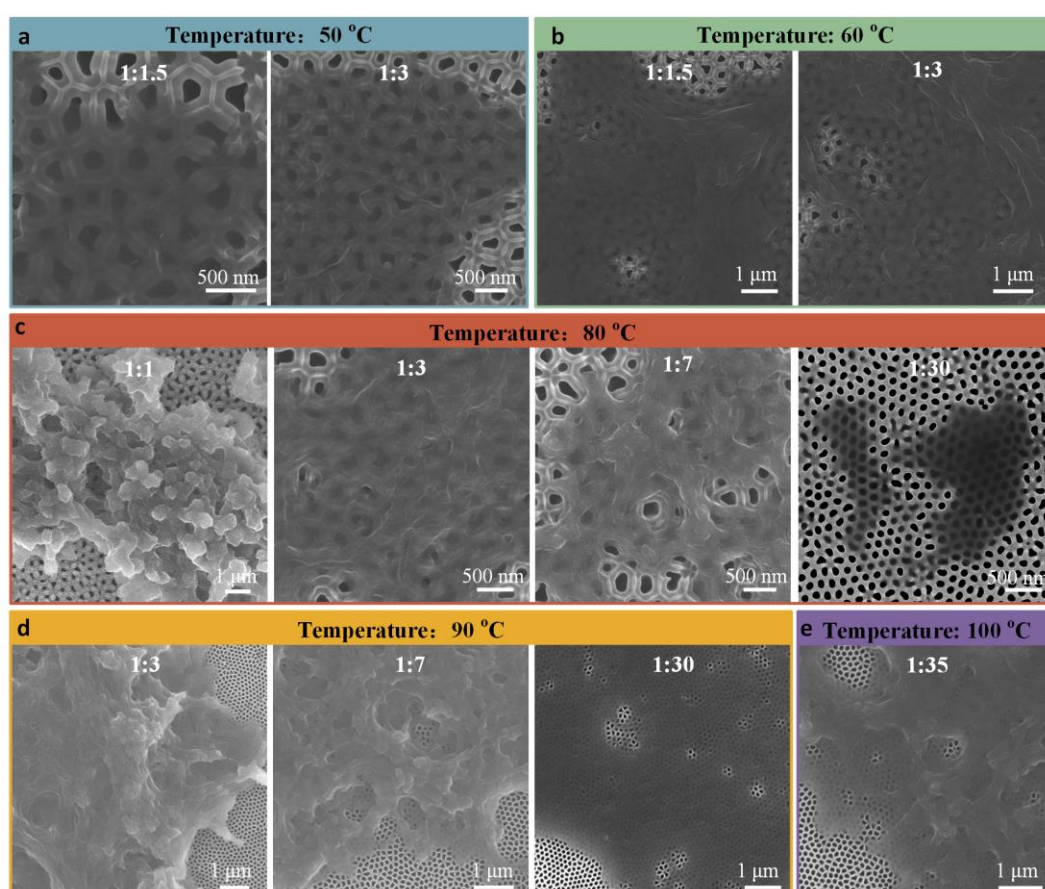
**Supplementary Fig. 15.** The SEM images of the CuBDC-(OH)$_2$ nanosheets prepared under different reaction conditions. Values of Cu/linker ratio and reaction temperature are given, with all reactions carried out for 30 min.
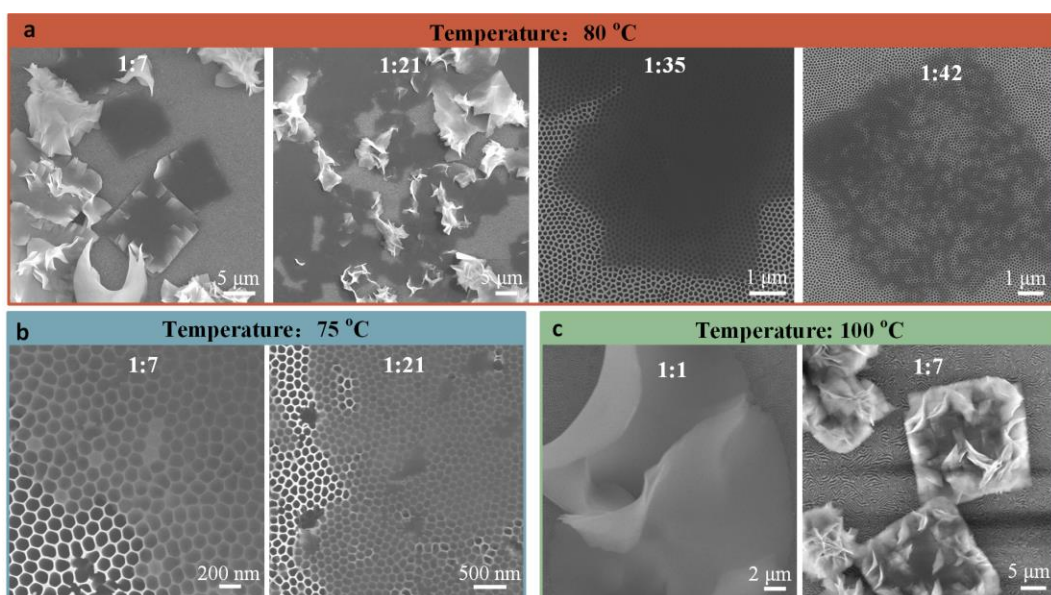
**Supplementary Fig. 16.** The SEM images of the CuBDC-NO$_2$ nanosheets prepared under different reaction conditions. Values of Cu/linker ratio and reaction temperature are given, with all reactions carried out for 30 min.
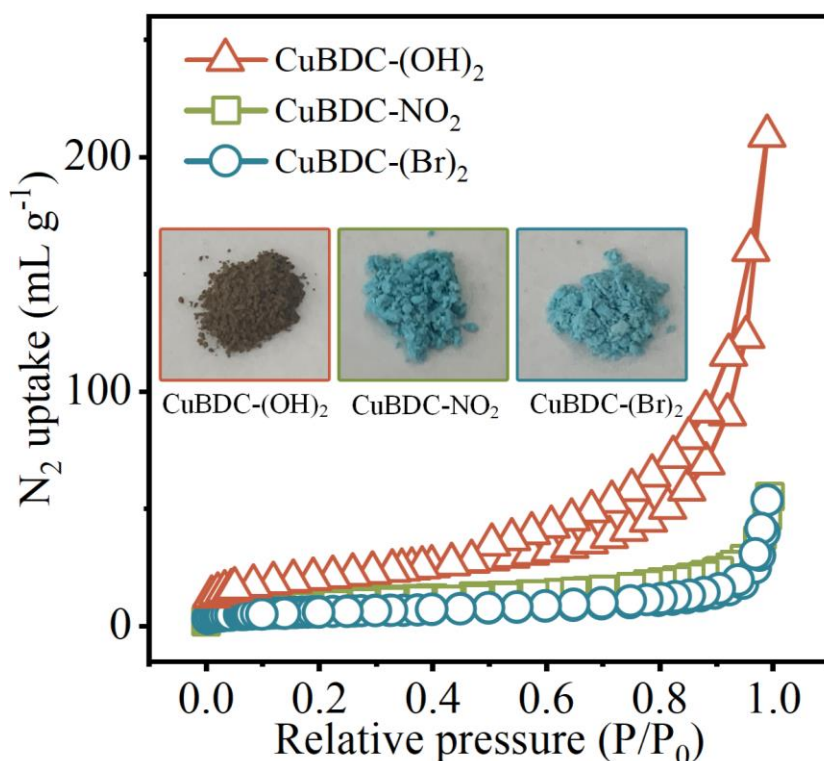
**Supplementary Fig. 17. Porous properties of MOF nanosheets.** $N_2$ adsorption-desorption isotherms (77 K) of CuBDC-(OH)$_2$, CuBDC-(Br)$_2$ and CuBDC-NO$_2$ nanosheets, corresponding photos of nanosheet powders. These MOF nanosheets exhibit typical features of microporous materials, with CuBDC-(Br)$_2$ and CuBDC-NO$_2$ showing smaller specific surface area compared to CuBDC-(OH)$_2$, possibly due to the incorporation of bulkier functional groups into the MOF structure.
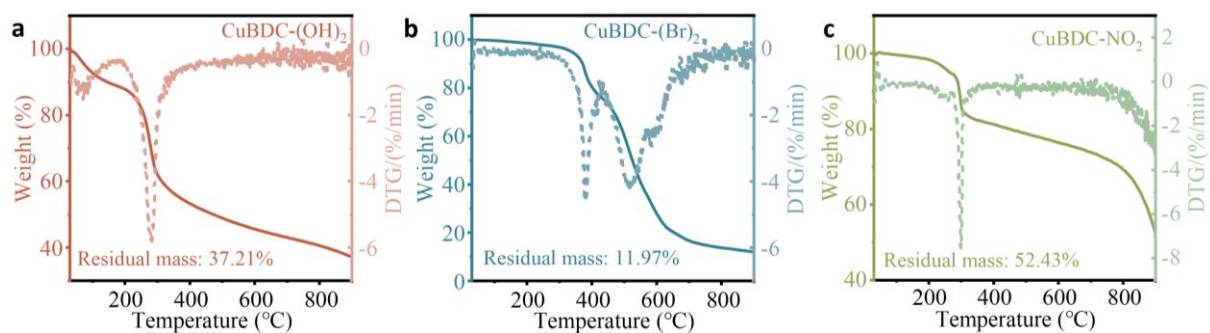
**Supplementary Fig. 18. Thermal stability of MOF nanosheets.** TG curves of (**a**) CuBDC-(OH)$_2$, (**b**) CuBDC-(Br)$_2$ and (**c**) CuBDC-NO$_2$ nanosheets.
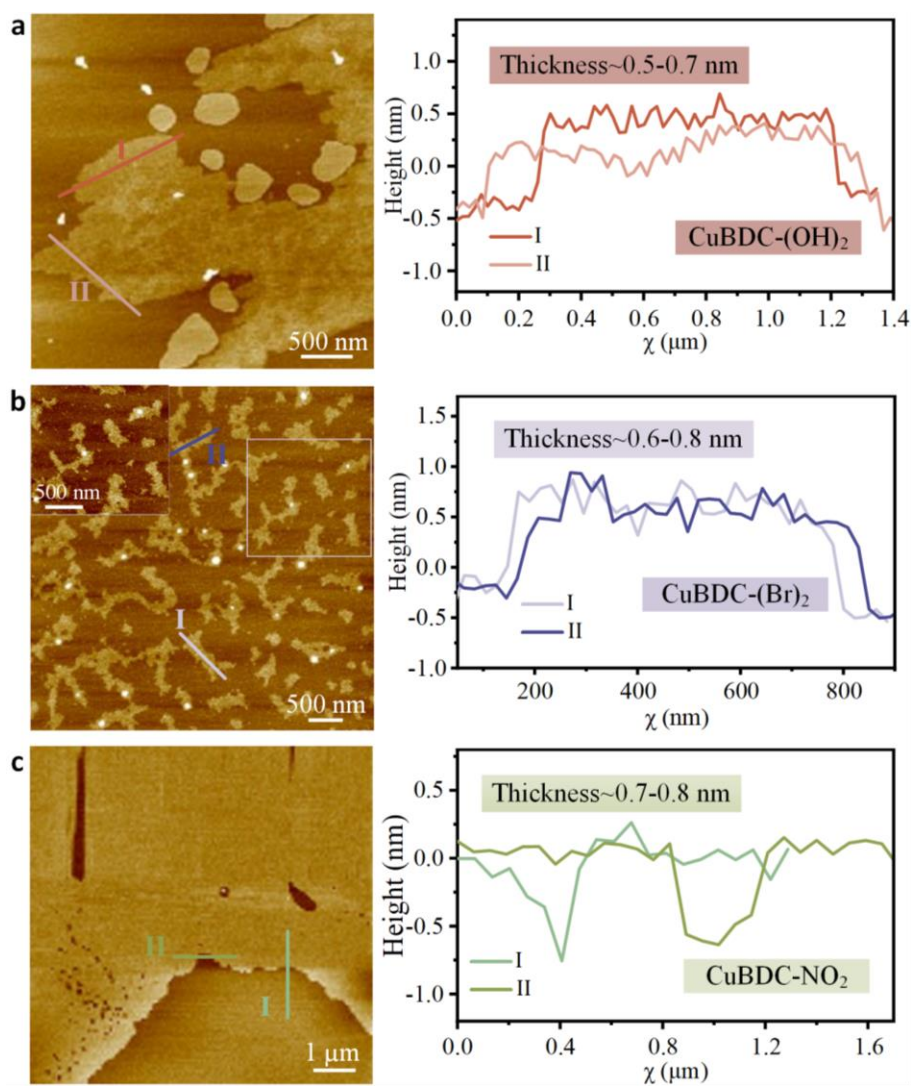
**Supplementary Fig. 19. AFM characterizations of MOF nanosheets.** AFM images of the (**a**) CuBDC-(OH)$_2$, (**b**) CuBDC-(Br)$_2$ and (**c**) CuBDC-NO$_2$ nanosheets. The height profiles of the nanosheets along the I and II lines were marked in the images.
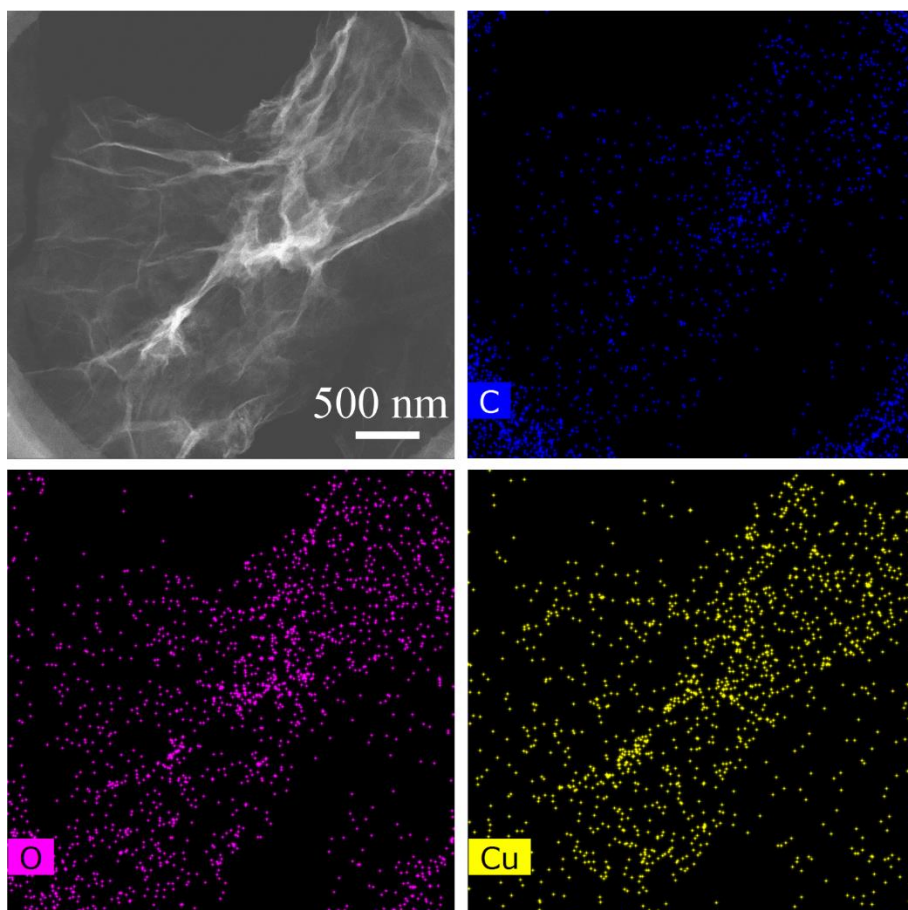
**Supplementary Fig. 20.** TEM and EDS images of the CuBDC-$(OH)_2$ nanosheets.
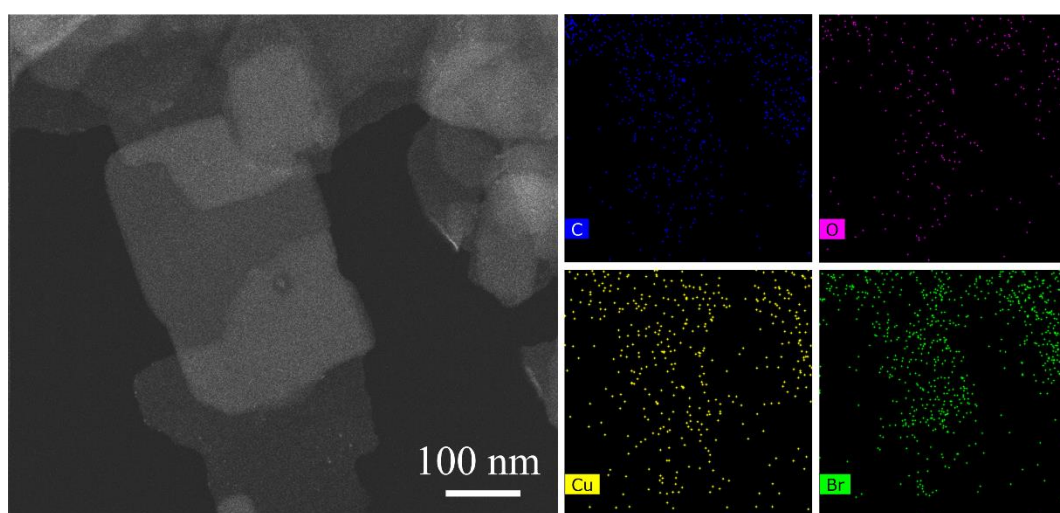
**Supplementary Fig. 21.** TEM and EDS images of the CuBDC-(Br)$_2$ nanosheets.
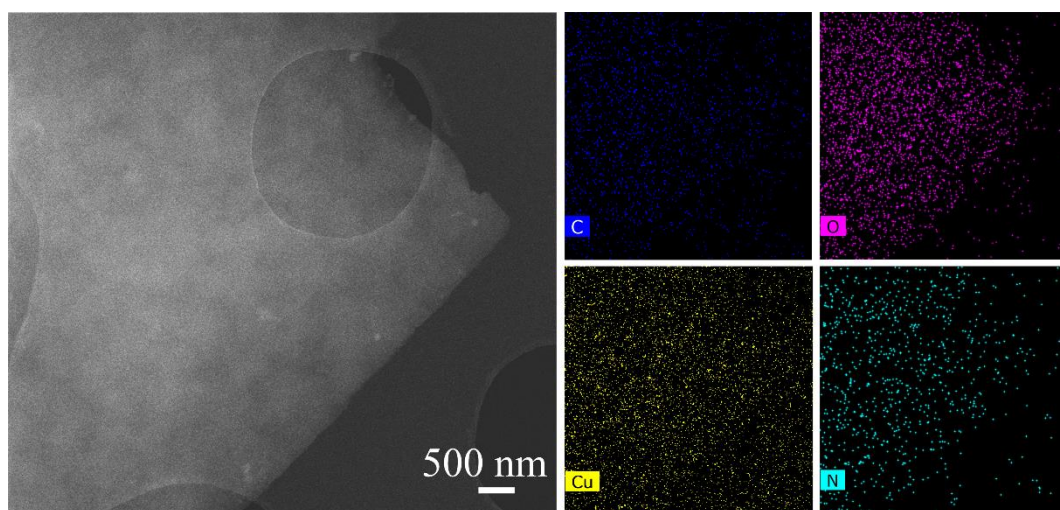
**Supplementary Fig. 22.** TEM and EDS images of the CuBDC-NO$_2$ nanosheets.
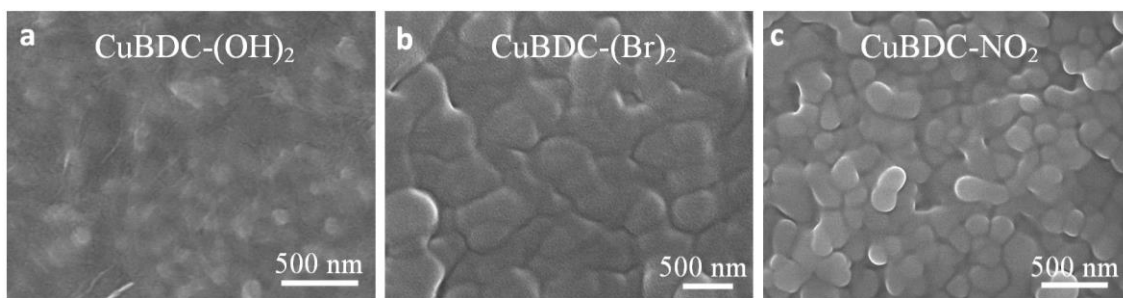
**Supplementary Fig. 23.** SEM surface images of the (**a**) CuBDC-$(OH)_2$, (**b**) CuBDC-$(Br)_2$ and (**c**) CuBDC-$NO_2$ nanosheet membranes.
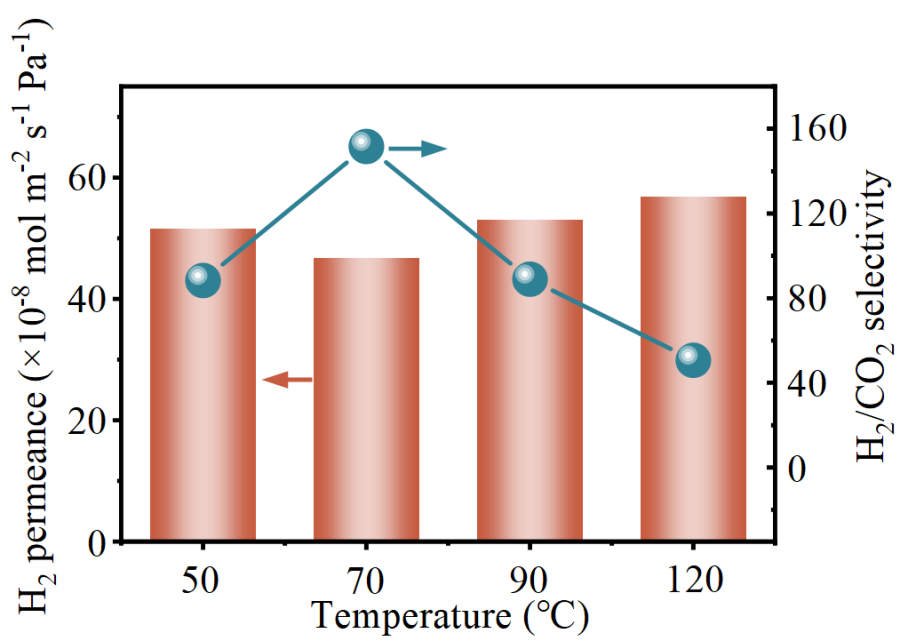
**Supplementary Fig. 24. Effect of drop-coating temperature on membrane separation performance.** $H_2/CO_2$ separation performance of the CuBDC-$(Br)_2$ nanosheet membrane prepared at various drop-coating temperatures.
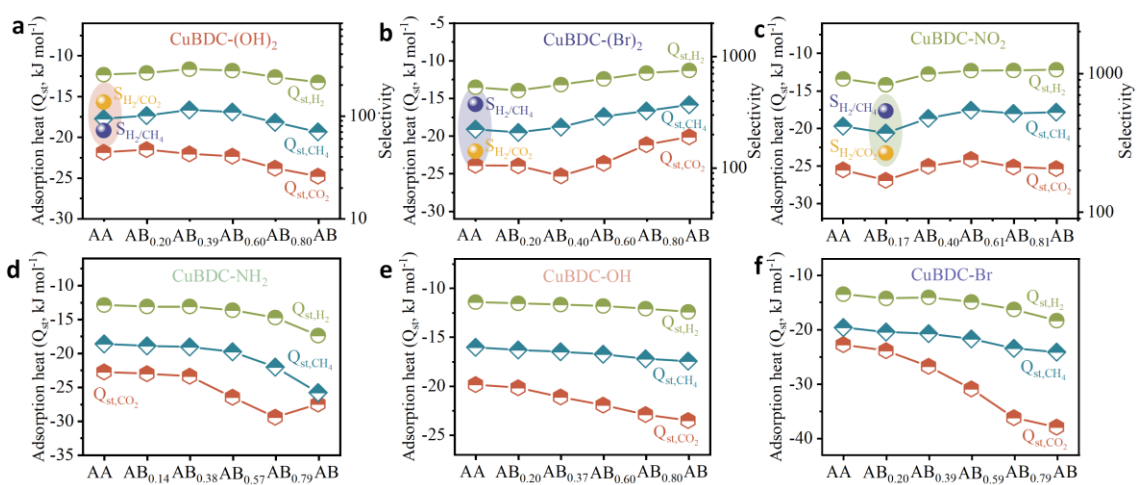
**Supplementary Fig. 25.** Isosteric heat of adsorptions ($Q_{st}$) at infinite dilution of $H_2$, $CH_4$ and $CO_2$ with (**a**) CuBDC-(OH)$_2$, (**b**) CuBDC-(Br)$_2$, (**c**) CuBDC-NO$_2$, (**d**) CuBDC-NH$_2$, (**e**) CuBDC-OH and (**f**) CuBDC-Br nanosheets in different stacking modes.
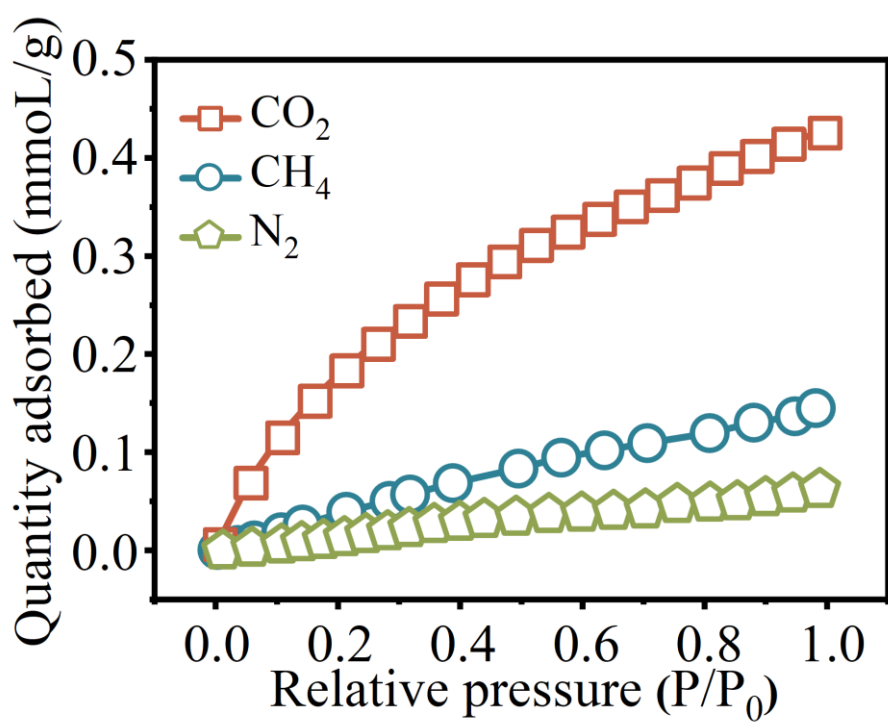
**Supplementary Fig. 26.** Gas adsorption isotherms of the CuBDC-NO$_2$ nanosheets measured experimentally at 25 ºC.
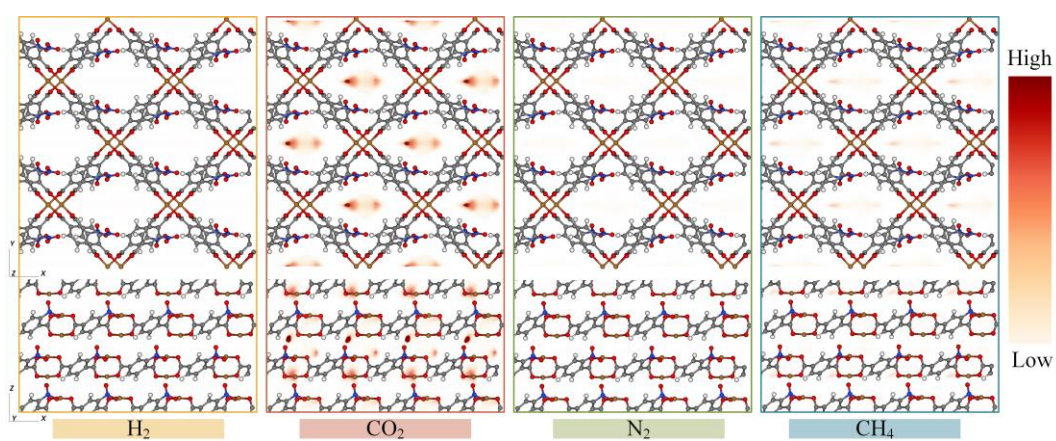
**Supplementary Fig. 27. 2D density distributions of H₂, CO₂, N₂ and CH₄ molecules within the CuBDC-NO₂ framework under ambient conditions.** Dark red and light yellow represent relatively high and low adsorption of different gas molecules by the framework, respectively. Cu, brown; O, red; N, blue; C, grey; H, white.
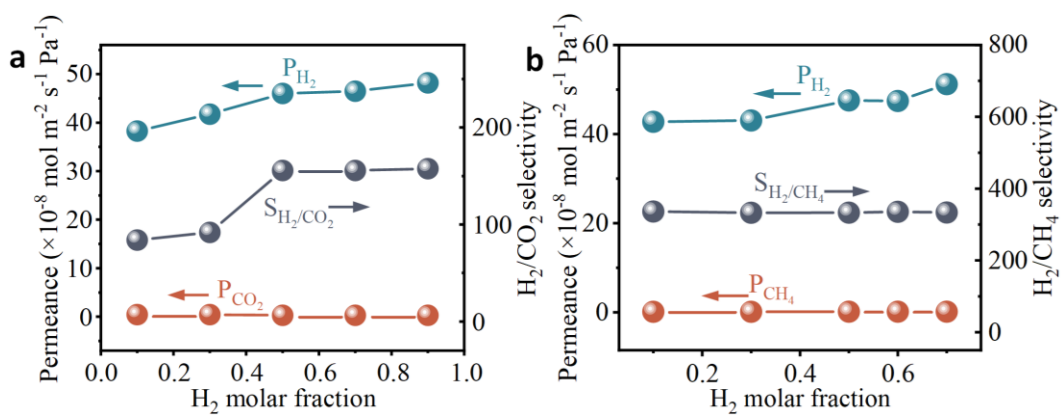
**Supplementary Fig. 28. Separation performance under different gas concentrations.** Gas separation performance of the CuBDC-(Br)$_2$ nanosheet membrane for (**a**) H$_2$/CO$_2$ and (**b**) H$_2$/CH$_4$ binary mixtures under various gas concentrations.
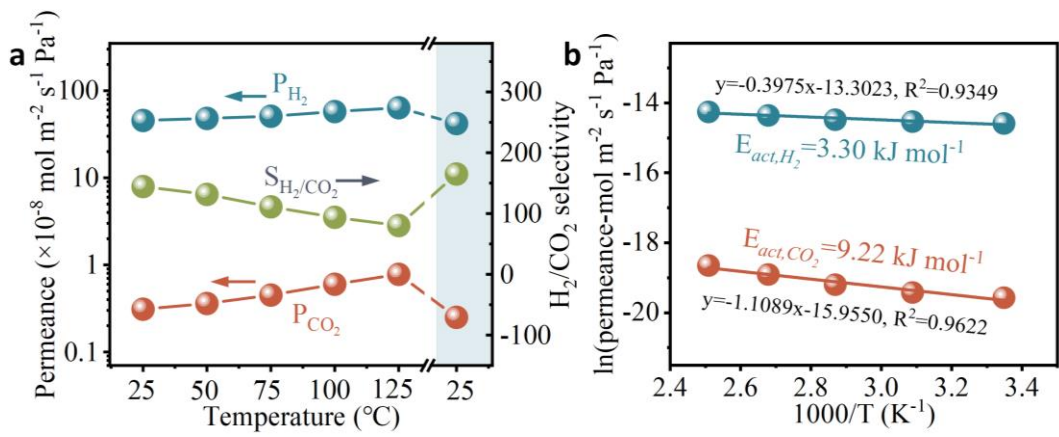
**Supplementary Fig. 29. Temperature-influenced transport of gas molecules within membranes. a,** $H_2/CO_2$ binary mixture separation performance of the CuBDC-(Br)$_2$ nanosheet membrane under various temperatures. The cyan area shows the performance of CuBDC-(Br)$_2$ membrane after recovering the temperature. **b,** Arrhenius temperature dependence of $H_2$ and $CO_2$ molecule permeation through the CuBDC-(Br)$_2$ nanosheets membrane. The temperature dependence is stated by Arrhenius equation:

$$P_i = A_i \exp\left(-\frac{E_{act,i}}{RT}\right) \tag{5}$$

$$\ln P_i = a - \frac{E_{act,i}}{R} \cdot \frac{1}{T} \tag{6}$$

$P_i$, $A_i$ and $E_{act,i}$ are the gas permeance, pre-exponential factor, and apparent activation energy of component i, respectively. R and T are the ideal gas constant and absolute temperature, respectively. The slope of the straight line based on $\ln(P_i)$ and $1/T$ is used to calculate $E_{act,i}$ The $E_{act,H_2}$ and $E_{act,CO_2}$ are 3.30 and 9.22 kJ mol$^{-1}$, respectively.
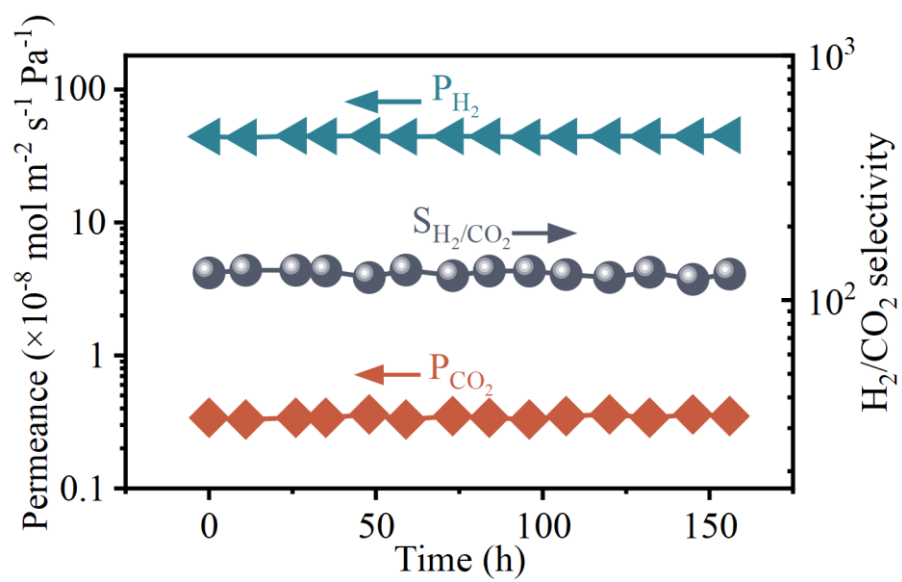
**Supplementary Fig. 30.** Long-term stability test of the CuBDC-(Br)$_2$ nanosheets membrane for H$_2$/CO$_2$ separation.
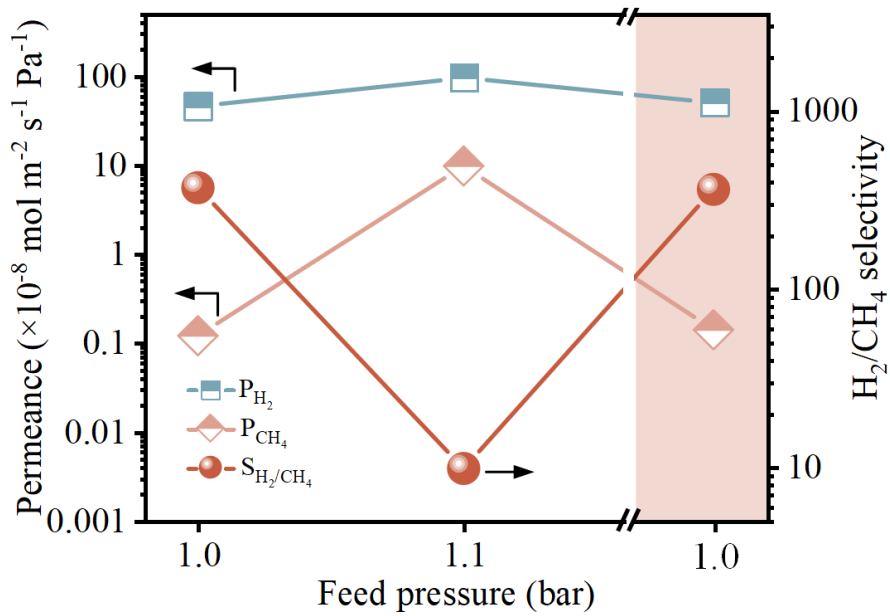
**Supplementary Fig. 31.** Gas separation performance of the CuBDC-(Br)$_2$ nanosheet membrane for H$_2$/CH$_4$ binary mixtures under different pressure conditions. The pink area show the performance of CuBDC-(Br)$_2$ nanosheet membrane after releasing the pressure.
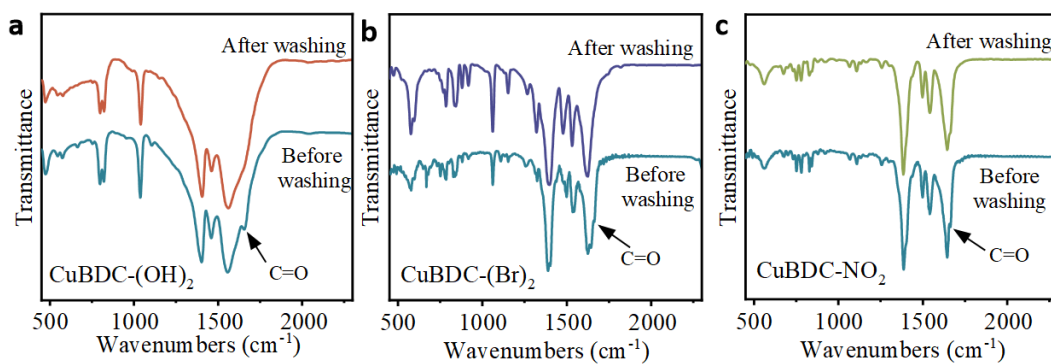
**Supplementary Fig. 32. FTIR spectra of the (a) CuBDC-(OH)₂, (b) CuBDC-(Br)₂ and (c) CuBDC-NO₂ nanosheets before and after washing.** To eliminate residual DMF solvent, the synthesized MOF nanosheets were repeatedly washed with $CH_2Cl_2$. A distinct peak at 1664 cm$^{-1}$ associated with the C=O stretching vibration of DMF solvent[24], can be observed in the nanosheets before washing, indicating the presence of DMF. After washing, the disappearance of such a peak confirms the complete removal of the solvent from the nanosheets.

**Supplementary Table 1 |** Crystal data and structure refinement parameters for bulk CuBDC-$(OH)_2$, CuBDC-$(Br)_2$, CuBDC-$NH_2$, CuBDC-$NO_2$, CuBDC-OH and CuBDC-Br.

| | CuBDC-$(OH)_2$ | CuBDC-$(Br)_2$ | CuBDC-$NH_2$ | CuBDC-$NO_2$ | CuBDC-OH | CuBDC-Br |
|---|---|---|---|---|---|---|
| Cell formula | $C_{32}H_{16}O_{24}$ $Cu_4$ | $C_{32}H_8O_{16}Cu_4$ $Br_8$ | $C_{32}H_{20}N_4O_{16}C$ $u_4$ | $C_{32}H_{12}N_4O_{24}C$ $u_4$ | $C_{32}H_{16}O_{20}C$ $u_4$ | $C_{32}H_{12}O_{16}Cu_4$ $Br_4$ |
| Space group | P 1 | P 1 | P 1 | P 1 | P 1 | P 1 |
| a/Å | 12.2635 | 13.6297 | 12.0026 | 11.3100 | 12.1228 | 11.8949 |
| b/Å | 14.3561 | 16.1374 | 14.6762 | 15.5497 | 15.6116 | 15.3380 |
| c/Å | 7.75877 | 5.16323 | 7.51277 | 8.03521 | 6.82440 | 8.13668 |
| $\alpha$ | 90.000 | 90.000 | 90.000 | 90.0018 | 90.000 | 90.000 |
| $\beta$ | 108.692 | 106.867 | 107.985 | 115.385 | 108.320 | 115.378 |
| $\gamma$ | 90.0000 | 90.0000 | 90.0000 | 89.9973 | 90.0000 | 90.0000 |
| Density (g cm$^{-3}$) | 1.33292 | 2.35579 | 1.28058 | 1.41855 | 1.31999 | 1.51816 |
| Cell Volume (Å$^3$) | 1293.93 | 1086.79 | 1258.73 | 1276.69 | 1226.10 | 1341.24 |
| Monolayer aperture (nm) | 0.7000 | 0.5804 | 0.6955 | 0.5452 | 0.7368 | 0.6506 |
| Monolayer thickness (nm) | 0.5479 | 0.6068 | 0.5975 | 0.5852 | 0.5307 | 0.5443 |
| *d*-spacing (nm) | 0.5422 | 0.4562 | 0.5266 | 0.5384 | 0.5137 | 0.5575 |

**Supplementary Table 2 |** Crystal data and structure refinement parameters of neighboring stacked CuBDC-$(OH)_2$ nanosheets with different stacking modes.

| | AA (most stable) | $AB_{0.20}$ | $AB_{0.39}$ | $AB_{0.60}$ | $AB_{0.80}$ | AB |
|---|---|---|---|---|---|---|
| Cell formula | | | $C_{64}H_{32}O_{48}Cu_8$ | | | |
| Space group | | | P 1 | | | |
| a/Å | 16.2740 | 16.1026 | 16.2174 | 16.2836 | 16.1017 | 16.0922 |
| b/Å | 14.5173 | 14.7042 | 14.5783 | 14.4764 | 14.6785 | 14.6884 |
| c/Å | 12.6613 | 13.1482 | 14.0229 | 13.9841 | 13.2686 | 12.8335 |
| $\alpha$ | 90.0000 | 90.0000 | 90.0000 | 90.0000 | 90.0000 | 90.0000 |
| $\beta$ | 90.0000 | 91.7430 | 87.8865 | 87.8253 | 92.6428 | 90.0000 |
| $\gamma$ | 90.0000 | 90.0000 | 90.0000 | 90.0000 | 90.0000 | 90.0000 |
| Density ($g\ cm^{-3}$) | 1.1532 | 1.1085 | 1.0412 | 1.0472 | 1.1011 | 1.1371 |
| Cell volume ($Å^3$) | 2991.29 | 3111.74 | 3313.07 | 3294.07 | 3132.68 | 3033.44 |
| Stacking aperture (nm) | 0.6409 | 0.5835 | 0.5532 | 0.5147 | 0.4256 | 0.3796 |
| $d$-spacing (nm) | 0.6331 | 0.6574 | 0.7011 | 0.6992 | 0.6634 | 0.6417 |
| Formation energy (eV/atom) | -0.0092 | 0.6006 | 0.8336 | 0.5880 | 0.5984 | 0.2541 |

**Supplementary Table 3 | Crystal data and structure refinement parameters of neighboring stacked CuBDC-(Br)$_2$ nanosheets with different stacking modes.**

| | AA (most stable) | AB$_{0.20}$ | AB$_{0.40}$ | AB$_{0.60}$ | AB$_{0.80}$ | AB |
|---|---|---|---|---|---|---|
| Cell formula | | | C$_{64}$H$_{16}$O$_{32}$Cu$_8$Br$_{16}$ | | | |
| Space group | | | P 1 | | | |
| a/Å | 14.3816 | 14.2383 | 14.2025 | 14.2133 | 14.0667 | 14.0213 |
| b/Å | 16.2786 | 16.4025 | 16.4449 | 16.4433 | 16.5588 | 16.6018 |
| c/Å | 12.2645 | 13.0977 | 13.9540 | 15.3026 | 16.3679 | 17.0070 |
| $\alpha$ | 90.0000 | 90.0000 | 90.0000 | 90.0000 | 90.0000 | 90.0000 |
| $\beta$ | 90.0000 | 90.1765 | 90.0675 | 90.9151 | 90.2480 | 90.0000 |
| $\gamma$ | 90.0000 | 90.0000 | 90.0000 | 90.0000 | 90.0000 | 90.0000 |
| Density (g cm$^{-3}$) | 1.7834 | 1.6740 | 1.5712 | 1.4319 | 1.3431 | 1.2934 |
| Cell volume (Å$^3$) | 2871.27 | 3058.87 | 32.59.08 | 3575.97 | 3812.50 | 3958.87 |
| Stacking aperture (nm) | 0.3791 | 0.2753 | 0.2513 | 0.1910 | 0.1670 | 0.1850 |
| $d$-spacing (nm) | 0.6132 | 0.6549 | 0.6977 | 0.7651 | 0.8184 | 0.8504 |
| Formation energy (eV/atom) | -0.0184 | 0.2008 | 0.4886 | 1.3562 | 1.6115 | 1.6174 |

**Supplementary Table 4 | Crystal data and structure refinement parameters of neighboring stacked CuBDC-$NH_2$ nanosheets with different stacking modes.**

| | AA | $AB_{0.14}$ (most stable) | $AB_{0.38}$ | $AB_{0.57}$ | $AB_{0.79}$ | AB |
|---|---|---|---|---|---|---|
| Cell formula | | | $C_{64}H_{40}N_8O_{32}Cu_8$ | | | |
| Space group | | | P 1 | | | |
| a/Å | 15.5602 | 15.2099 | 14.8246 | 14.3825 | 14.1134 | 13.3652 |
| b/Å | 15.1342 | 15.4908 | 15.8686 | 16.2357 | 16.4711 | 17.0134 |
| c/Å | 11.1370 | 10.5733 | 11.4698 | 11.4196 | 10.3241 | 9.0121 |
| $\alpha$ | 90.0000 | 90.0000 | 90.0000 | 90.0000 | 90.0000 | 90.0000 |
| $\beta$ | 90.0000 | 91.1522 | 87.8291 | 88.2999 | 89.1432 | 90.0000 |
| $\gamma$ | 90.0000 | 90.0000 | 90.0000 | 90.0000 | 90.0000 | 90.0000 |
| Density (g cm$^{-3}$) | 1.2292 | 1.2943 | 1.1957 | 1.2095 | 1.3434 | 1.5732 |
| Cell volume (Å$^3$) | 2622.67 | 2490.71 | 2696.28 | 2665.42 | 2399.71 | 2049.24 |
| Stacking aperture (nm) | 0.6116 | 0.5384 | 0.4472 | 0.3524 | 0.2747 | 0.2522 |
| d-spacing (nm) | 0.5568 | 0.5287 | 0.5735 | 0.5710 | 0.5162 | 0.4506 |
| Formation energy (eV/atom) | -0.0170 | -0.1448 | 1.0985 | 1.8113 | 1.2161 | 0.1289 |

**Supplementary Table 5 | Crystal data and structure refinement parameters of neighboring stacked CuBDC-NO$_2$ nanosheets with different stacking modes.**

| | AA | AB$_{0.17}$ (most stable) | AB$_{0.40}$ | AB$_{0.61}$ | AB$_{0.81}$ | AB |
|---|---|---|---|---|---|---|
| Cell formula | | | C$_{64}$H$_{24}$N$_8$O$_{48}$Cu$_8$ | | | |
| Space group | | | P 1 | | | |
| a/Å | 14.6890 | 15.0294 | 15.0057 | 14.9050 | 14.7812 | 14.8927 |
| b/Å | 15.9169 | 15.6200 | 15.6747 | 15.7714 | 15.8793 | 15.7865 |
| c/Å | 10.8875 | 10.2859 | 12.7289 | 13.5234 | 13.2732 | 13.4612 |
| $\alpha$ | 90.0000 | 89.9965 | 90.0000 | 89.9995 | 90.0002 | 90.0000 |
| $\beta$ | 90.0000 | 88.8476 | 86.6114 | 85.8347 | 91.8289 | 90.0000 |
| $\gamma$ | 89.9999 | 89.9997 | 89.9997 | 90.0000 | 90.0000 | 89.9999 |
| Density (g cm$^{-3}$) | 1.4229 | 1.5003 | 1.2119 | 1.1424 | 1.1632 | 1.1445 |
| Cell volume (Å$^3$) | 2545.53 | 2414.22 | 2988.73 | 3170.59 | 3113.83 | 3164.78 |
| Stacking aperture (nm) | 0.4830 | 0.3721 | 0.3681 | 0.3643 | 0.3574 | 0.3524 |
| d-spacing (nm) | 0.5444 | 0.5143 | 0.6364 | 0.6762 | 0.6637 | 0.6731 |
| Formation energy (eV/atom) | -0.0183 | -0.7774 | 0.8673 | 0.8930 | 0.9966 | 1.2437 |

**Supplementary Table 6 | Crystal data and structure refinement parameters of neighboring stacked CuBDC-OH nanosheets with different stacking modes.**

| | AA | $AB_{0.20}$ | $AB_{0.37}$ (most stable) | $AB_{0.60}$ | $AB_{0.80}$ | AB |
|---|---|---|---|---|---|---|
| Cell formula | | | $C_{64}H_{32}O_{40}Cu_8$ | | | |
| Space group | | | P 1 | | | |
| a/Å | 15.0611 | 15.1138 | 15.1592 | 15.2070 | 15.2544 | 15.3001 |
| b/Å | 15.6762 | 15.6352 | 15.5954 | 15.5496 | 15.5029 | 15.4580 |
| c/Å | 13.2251 | 13.2238 | 13.1892 | 13.2214 | 13.2588 | 13.2273 |
| $\alpha$ | 90.0000 | 90.0000 | 90.0000 | 90.0000 | 90.0000 | 90.0000 |
| $\beta$ | 90.0000 | 90.0021 | 90.0408 | 89.9994 | 90.0532 | 90.0000 |
| $\gamma$ | 90.0000 | 90.0000 | 90.0000 | 90.0000 | 90.0000 | 90.0000 |
| Density (g cm$^{-3}$) | 1.0366 | 1.0358 | 1.0381 | 1.0354 | 1.0323 | 1.0347 |
| Cell volume (Å$^3$) | 3122.46 | 3124.88 | 3118.11 | 3126.37 | 3135.54 | 3128.37 |
| Stacking aperture (nm) | 0.7279 | 0.6830 | 0.5949 | 0.5162 | 0.4501 | 0.3990 |
| d-spacing (nm) | 0.6613 | 0.6612 | 0.6595 | 0.6611 | 0.6629 | 0.6614 |
| Formation energy (eV/atom) | -0.0083 | -0.0461 | -0.1135 | 0.1206 | 0.2306 | 0.0975 |

**Supplementary Table 7 | Crystal data and structure refinement parameters of neighboring stacked CuBDC-Br nanosheets with different stacking modes.**

| | AA | $AB_{0.20}$ | $AB_{0.39}$ | $AB_{0.59}$ | $AB_{0.79}$ | AB (most stable) |
|---|---|---|---|---|---|---|
| Cell formula | | | $C_{64}H_{24}O_{32}Cu_8Br_8$ | | | |
| Space group | | | P 1 | | | |
| a/Å | 15.2380 | 15.3268 | 14.9642 | 14.7839 | 146650 | 14.3400 |
| b/Å | 15.4235 | 15.3780 | 15.6904 | 15.8577 | 15.9991 | 16.3123 |
| c/Å | 11.0542 | 10.4466 | 10.8060 | 10.5116 | 9.6847 | 8.6445 |
| $\alpha$ | 90.0000 | 90.0000 | 90.0000 | 90.0000 | 90.0000 | 90.0000 |
| $\beta$ | 90.0000 | 88.5687 | 89.5930 | 90.4934 | 87.9073 | 90.0000 |
| $\gamma$ | 90.0000 | 90.0000 | 90.0000 | 90.0000 | 90.0000 | 90.0000 |
| Density ($g\ cm^{-3}$) | 1.5675 | 1.6545 | 1.6051 | 1.6526 | 1.7934 | 2.0139 |
| Cell volume ($Å^3$) | 2597.99 | 2461.45 | 2537.12 | 2464.23 | 2270.77 | 2022.11 |
| Stacking aperture (nm) | 0.4962 | 0.3892 | 0.3324 | 0.2931 | 0.2362 | 0.2284 |
| d-spacing (nm) | 0.5527 | 0.5223 | 0.5403 | 0.5256 | 0.4842 | 0.4322 |
| Formation energy (eV/atom) | -0.0159 | -0.3489 | 0.2964 | 0.8128 | 0.1701 | -0.7286 |

**Supplementary Table 8 |** Porous properties of the CuBDC-(OH)$_2$, CuBDC-(Br)$_2$ and CuBDC-NO$_2$ nanosheets.

| MOF nanosheets | BET surface area (m$^2$ g$^{-1}$) |
|---|---|
| CuBDC-(OH)$_2$ | 66.56 |
| CuBDC-(Br)$_2$ | 20.01 |
| CuBDC-NO$_2$ | 36.14 |

**Supplementary Table 9 |** Gas separation performance of the CuBDC-(Br)$_2$ nanosheets membranes prepared at various drop-coating temperatures for H$_2$/CH$_4$ binary mixture.

| Tempareture (ºC) | Sample | H$_2$ permeance ($\times 10^{-8}$ mol m$^{-2}$ s$^{-1}$ Pa$^{-1}$) | H$_2$/CH$_4$ |
|---|---|---|---|
| 50 | M1 | 53.34 | 278.0 |
| | M2 | 54.24 | 276.1 |
| | M3 | 51.32 | 271.8 |
| | Average | 52.97 | 275.3 |
| 70 | M1 | 46.50 | 357.5 |
| | M2 | 47.56 | 356.8 |
| | M3 | 45.86 | 371.1 |
| | Average | 46.64 | 361.8 |
| 90 | M1 | 53.64 | 259.5 |
| | M2 | 51.00 | 253.1 |
| | M3 | 53.08 | 245.7 |
| | Average | 52.57 | 252.8 |
| 120 | M1 | 59.01 | 165.6 |
| | M2 | 60.46 | 209.4 |
| | M3 | 63.91 | 194.4 |
| | Average | 61.13 | 189.8 |

**Supplementary Table 10 |** Gas permeation properties and ideal selectivity of the CuBDC-$(OH)_2$, CuBDC-$(Br)_2$ and CuBDC-$NO_2$ nanosheets membranes.

| Sample | | Permeance ($\times 10^{-8}$ mol m$^{-2}$ s$^{-1}$ Pa$^{-1}$) | | | | Ideal selectivity | | |
|---|---|---|---|---|---|---|---|---|
| | | $H_2$ | $CO_2$ | $N_2$ | $CH_4$ | $H_2/CO_2$ | $H_2/N_2$ | $H_2/CH_4$ |
| CuBDC-$(OH)_2$ | M1 | 55.82 | 0.36 | 0.69 | 0.65 | 154.3 | 80.7 | 86.3 |
| | M2 | 57.51 | 0.42 | 0.80 | 0.70 | 138.2 | 72.2 | 82.6 |
| | M3 | 58.86 | 0.42 | 0.85 | 0.69 | 141.5 | 69.1 | 85.7 |
| | Average | 57.40 | 0.40 | 0.78 | 0.68 | 144.7 | 74.0 | 84.9 |
| CuBDC-$(Br)_2$ | M1 | 52.08 | 0.23 | 0.29 | 0.12 | 222.8 | 179.4 | 423.9 |
| | M2 | 52.46 | 0.27 | 0.34 | 0.12 | 191.5 | 156.2 | 447.6 |
| | M3 | 48.23 | 0.25 | 0.29 | 0.10 | 190.3 | 168.0 | 465.7 |
| | Average | 50.92 | 0.25 | 0.31 | 0.11 | 201.5 | 167.9 | 445.7 |
| CuBDC-$NO_2$ | M1 | 46.36 | 0.13 | 0.11 | 0.073 | 353.7 | 417.2 | 637.0 |
| | M2 | 49.40 | 0.13 | 0.11 | 0.076 | 368.6 | 440.8 | 648.5 |
| | M3 | 46.90 | 0.13 | 0.11 | 0.072 | 368.9 | 443.5 | 647.0 |
| | Average | 47.55 | 0.13 | 0.11 | 0.074 | 363.7 | 433.8 | 644.2 |

**Supplementary Table 11.** Gas separation performance of the CuBDC-(OH)$_2$, CuBDC-(Br)$_2$ and CuBDC-NO$_2$ nanosheets membranes for H$_2$/CO$_2$ and H$_2$/CH$_4$ binary mixture.

| 2D MOF membranes | Sample | H$_2$ permeance (H$_2$/CO$_2$ binary mixture) ($\times10^{-8}$ mol m$^{-2}$ s$^{-1}$ Pa$^{-1}$) | $S_{H_2/CO_2}$ | H$_2$ permeance (H$_2$/CH$_4$ binary mixture) ($\times10^{-8}$ mol m$^{-2}$ s$^{-1}$ Pa$^{-1}$) | $S_{H_2/CH_4}$ |
|---|---|---|---|---|---|
| CuBDC-(OH)$_2$ | M1 | 53.55 | 152.5 | 54.64 | 81.4 |
| | M2 | 56.44 | 132.6 | 56.29 | 77.2 |
| | M3 | 57.15 | 135.3 | 59.42 | 71.5 |
| | Average | 55.71 | 140.1 | 56.78 | 76.7 |
| CuBDC-(Br)$_2$ | M1 | 46.70 | 142.8 | 46.50 | 357.5 |
| | M2 | 43.65 | 140.0 | 45.86 | 371.1 |
| | M3 | 46.70 | 151.7 | 47.56 | 356.8 |
| | Average | 45.68 | 144.9 | 46.64 | 361.8 |
| CuBDC-NO$_2$ | M1 | 40.56 | 243.0 | 42.11 | 515.1 |
| | M2 | 41.56 | 252.2 | 44.84 | 489.2 |
| | M3 | 42.01 | 265.5 | 44.40 | 535.6 |
| | Average | 41.38 | 253.6 | 43.78 | 515.3 |

## Supplementary References

1. Kresse, G., Furthmüller, J. Efficient iterative schemes for ab initio total-energy calculations using a plane-wave basis set. Phys. Rev. B **54**, 11169-86 (1996).

2. Kresse, G., Furthmüller, J. Efficiency of ab-initio total energy calculations for metals and semiconductors using a plane-wave basis set. Comp. Mater. Sci. **6**, 15-50 (1996).

3. Perdew, J. P., Burke, K., Ernzerhof, M. Generalized gradient approximation made simple. Phys. Rev. Lett. **77**, 3865-8 (1996).

4. Grimme, S., Ehrlich, S., Goerigk, L. Effect of the damping function in dispersion corrected density functional theory. J. Comput. Chem. **32**, 1456-65 (2011).

5. Sun, Y. et al. High-rate nanofluidic energy absorption in porous zeolitic frameworks. Nat. Mater. **20**, 1015-1023 (2021).

6. Hajek, J. et al. Mechanistic studies of aldol condensations in UiO-66 and UiO-66-$NH_2$ metal organic frameworks. J. Catal. **331**, 1-12 (2015).

7. Verploegh, R. J. et al. Screening diffusion of small molecules in flexible zeolitic imidazolate frameworks using a DFT-parameterized force field. J. Phys. Chem. C **123**, 9153-9167 (2019).

8. Gee, J. A., Sholl, D. S. Prediction of adsorption properties of cyclic hydrocarbons in MOFs using DFT-derived force fields. J. Phys. Chem. C **119**, 16920-16926 (2015).

9. Ghanavati, R., Escobosa, A. C., Manz T. A. An automated protocol to construct flexibility parameters for classical forcefields: applications to metal-organic frameworks. RSC Adv. **14**, 22714-22762 (2024).

10. Rosen, A. S. et al. Machine learning the quantum-chemical properties of metal-organic frameworks for accelerated materials discovery. Matter **4**, 1578-1597 (2021).

11. Rosen, A. S. et al. High-throughput predictions of metal-organic framework electronic properties: theoretical challenges, graph neural networks, and data exploration. npj Comput. Mater. **8**, 112 (2022).

12. Henkelman, G., Uberuaga, B. P., Jónsson, H. A climbing image nudged elastic band method for finding saddle points and minimum energy paths. J. Chem. Phys. **113**, 9901-4 (2000).

13. Widom, B. Some topics in the theory of fluids. J. Chem. Phys. **39**, 2808-2812 (1963).

14. Dubbeldam, D. et al. RASPA: molecular simulation software for adsorption and diffusion in flexible nanoporous materials. Mol. Simulat. **42**, 81-101 (2015).

15. Ewald, P. P. Die Berechnung optischer und elektrostatischer Gitterpotentiale. Ann. Phys. **369**, 253-287 (1921).

16. Coupry, D. E., Addicoat, M. A., Heine, T. Extension of the universal force field for metal-organic frameworks. J. Chem. Theory Comput. **12**, 5215-5225 (2016).

17. Addicoat, M. A. et al. Extension of the universal force field to metal-organic frameworks. J. Chem. Theory Comput. **10**, 880-891 (2014).

18. Manz, T. A., Gabaldon Limas, N. Introducing DDEC6 atomic population analysis: part 1. Charge partitioning theory and methodology. RSC Adv. **6**, 47771-47801 (2016).

19. Martin, M. G., Ilja Siepmann, J. Transferable potentials for phase equilibria. 1. United-atom description of n-Alkanes. J. Phys. Chem. B **102**, 2569-2577 (1998).

20. Sun, Y. et al. Fingerprinting diverse nanoporous materials for optimal hydrogen storage conditions using meta-learning. Sci. Adv. **7**, eabg3983 (2021).

21. Lu, T., Chen, F. Multiwfn: A multifunctional wavefunction analyzer. J. Comput. Chem. **33**, 580-92 (2012).

22. Willems, T. F. Algorithms and tools for high-throughput geometry-based analysis of crystalline porous materials. Micropor. Mesopor. Mater. **149**, 134-141 (2012).

23. Zou, X., Hovmöller, S., Oleynikov, P. Electron crystallography: electron microscopy and electron diffraction. Oxford University Press, **16**, (2011).

24. Wang, S. et al. Fabrication of mesoporous MOF nanosheets via surfactant-template method for C-S coupling reactions. Micropor. Mesopor. Mat. **303**, 110254 (2020).